

2012-01-01

Development of Advanced Polymer Nanocomposite Capacitors

Miguel Mendoza

University of Texas at El Paso, mmendoza11@miners.utep.edu

Follow this and additional works at: https://digitalcommons.utep.edu/open_etd

 Part of the [Materials Science and Engineering Commons](#), [Mechanics of Materials Commons](#), and the [Nanoscience and Nanotechnology Commons](#)

Recommended Citation

Mendoza, Miguel, "Development of Advanced Polymer Nanocomposite Capacitors" (2012). *Open Access Theses & Dissertations*. 1883.
https://digitalcommons.utep.edu/open_etd/1883

This is brought to you for free and open access by DigitalCommons@UTEP. It has been accepted for inclusion in Open Access Theses & Dissertations by an authorized administrator of DigitalCommons@UTEP. For more information, please contact lweber@utep.edu.

DEVELOPMENT OF ADVANCED POLYMER NANOCOMPOSITE CAPACITORS

MIGUEL MENDOZA

Department of Mechanical Engineering

APPROVED:

Yirong Lin, Ph.D., Chair

Bill Tseng, Ph.D.

Chintalapalle Ramana, Ph.D.

Norman Love Jr., Ph.D.

Benjamin C. Flores, Ph.D.
Dean of the Graduate School

Copyright ©

by

Miguel Mendoza

2012

Dedication

To my parents, Gloria and Miguel, my sister Tania, and my girlfriend Andrea.

DEVELOPMENT OF ADVANCED POLYMER NANOCOMPOSITE CAPACITORS

by

MIGUEL MENDOZA, B.S. in M. E.

THESIS

Presented to the Faculty of the Graduate School of

The University of Texas at El Paso

in Partial Fulfillment

of the Requirements

for the Degree of

MASTER OF SCIENCE

Department of Mechanical Engineering

THE UNIVERSITY OF TEXAS AT EL PASO

December 2012

Acknowledgements

First, I would like to extend my sincere gratitude to my mentor Dr. Yirong Lin for his continued guidance, patience, motivation, and support throughout my graduate studies. I really appreciate your constant encouragement and advice during all these countless hours of research. Thanks for offering me the opportunity of conducting high quality research and discovering the marvelous field of nanomaterials. I could not have imagined having a better advisor during my graduate career. I would also like to extend this immense gratitude to the rest of my thesis committee members: Dr. Chintalapalle Ramana, Dr. Norman Love Jr., and Dr. Bill Tseng. Thanks for your constant advice and support through the fulfillment of this academic degree.

None of this research would have been possible without the support and sponsorship from the University of Texas at El Paso (UTEP), the Department of Mechanical Engineering (UTEP), and the center for Space Exploration Technology Research (cSETR). I would like to thank my fellow labmates Md Ashiqur Rahaman Khan, Mohammad Arif Ishtiaque Shuvo, Travis Wilson, and Philip Morton for sharing their knowledge and experiences with me, as well as for their continuous cooperation. Special thanks to Diego Delfin for his enormous effort, dedication, enthusiasm, and for spending numerous hours with me in the lab in order to ensure the success of this research. I would also like to thank to Salvador M. Rodriguez, Jesus F. Hinojos, Ernesto J. Rubio, Gustavo Martinez, and Arturo Acosta for sharing their knowledge in SEM and XRD and for their continuous support and encouragement throughout my graduate studies.

Finally, I would like to recognize the immense support provided by my family. Thanks to my parents, sister, and relatives for their inspiration, patience, and advice. None of these would have been possible without your encouragement and guidance. I am who I am because of your infinite love and support. I would also like to thank to Andrea Galicia, my girlfriend, for her enthusiasm and motivation in order to overcome all those challenges faced during my graduate career. I love you and I really appreciate your patience and support.

Abstract

The current development of modern electronics has driven the need for new series of energy storage devices with higher energy density and faster charge/discharge rate. Batteries and capacitors are two of the most widely used energy storage devices. Compared with batteries, capacitors have higher power density and significant higher charge/discharge rate. Therefore, high energy density capacitors play a significant role in modern electronic devices, power applications, space flight technologies, hybrid electric vehicles, portable defibrillators, and pulse power applications. Dielectric film capacitors represent an exceptional alternative for developing high energy density capacitors due to their high dielectric constants, outstanding breakdown voltages, and flexibility. The implementation of high aspect ratio dielectric inclusions such as nanowires into polymer capacitors could lead to further enhancement of its energy density. Therefore, this research effort is focused on the development of a new series of dielectric capacitors composed of nanowire reinforced polymer matrix composites. This concept of nanocomposite capacitors combines the extraordinary physical and chemical properties of the one-dimension (1D) nanoceramics and high dielectric strength of polymer matrices, leading to a capacitor with improved dielectric properties and energy density.

Lead-free sodium niobate (NaNbO_3) and lead-containing lead magnesium niobate-lead titanate (0.65PMN-0.35PT) nanowires were synthesized following hydrothermal and sol-gel approaches, respectively. The as-prepared nanowires were mixed with a polyvinylidene fluoride (PVDF) matrix using solution-casting method for nanocomposites fabrication. The dielectric constants and breakdown voltages of the $\text{NaNbO}_3/\text{PVDF}$ and 0.65PMN-0.35PT/PVDF nanocomposites were measured under different frequency ranges and temperatures in order to determine their maximum energy (J/cm^3) and specific (J/g) densities. The electrical properties of the synthesized nanoceramics were compared with commercially available barium titanate

(BaTiO₃) and lead zirconate titanate Pb(Zr_xTi_{1-x})O₃ powders embedded into a PVDF matrix. The resulting dielectric film capacitors represent an excellent alternative energy storage device for future high energy density applications.

Table of Contents

Acknowledgements	v
Abstract	vi
Table of Contents	viii
List of Tables	ix
List of Figures	x
Chapter 1: Introduction	1
1.1 Overview	1
1.2 Objective	13
Chapter 2: Literature Review	15
2.1 Capacitors.....	15
2.2 The Perovskite Structure.....	16
2.3 Synthesis of 1-D Nanostructures	19
2.4 Nanocomposites.....	22
Chapter 3: Methodology	23
3.1 Synthesis of Nanowires.....	23
3.2 Preparation of Nanocomposites	27
3.3 Samples Characterization.....	28
3.4 Electrical Testing	28
Chapter 4: Results and Discussion.....	31
4.1 Sample Characterization	31
4.2 Electrical Properties of Nanocomposites	36
Chapter 5: Conclusion.....	49
References.....	50
Vita.....	55

List of Tables

Table 1.1. Operation parameters and energy density values for current advanced capacitor systems [18].	8
Table 1.2. Common electrical properties of polymer-based capacitors [18].	9
Table 1.3. Dielectric permittivity values for commonly employed engineering ceramics [25]. ..	10

List of Figures

Figure 1.1. Ragone plot of various energy storage devices displaying their power and energy densities [6].	2
Figure 1.2. The Leyden jar, which is known as the first capacitor in history: (a) digital picture view [3] and (b) schematic cross-section view.	3
Figure 1.3: Schematic diagram of a single-cell double layer capacitor [13].	5
Figure 1.4. Commercial polymer-based dielectric capacitors: (a) digital picture view, and (b) schematic cross-sectional view.	9
Figure 1.5. Commercial multilayer ceramic capacitors: (a) digital view and (b) schematic cross-sectional view [26].	11
Figure 1.6. Common 1-D nanostructures previously synthesized by several research groups: (a) nanowires, (b) nanorods, and (c) nanotubes [32].	12
Figure 1.7. Schematic diagram for an advanced nanocomposite capacitor capable combining electrical properties of both polymer and ceramic-based capacitors.	13
Figure 2.1. Schematic presentation of the main components of an electrostatic capacitor.	15
Figure 2.2. The ideal perovskite cubic closed-packed unit cell [22].	17
Figure 3.1. Schematic diagram for the developed electrospinning setup.	26
Figure 3.2. Schematic diagram showing the location of the heat source employed during the electrospinning.	26
Figure 3.3. Schematic diagram of the manufacturing process of $\text{NaNbO}_3/\text{PVDF}$ nanocomposites.	27
Figure 3.4. Sample characterization facilities available at the University of Texas at El Paso: (a) SEM and (b) XRD.	28
Figure 3.5. Schematic diagram for the frequency dependent capacitance testing.	29
Figure 3.6. Schematic diagram for the breakdown strength testing setup.	30
Figure 4.1. XRD patterns for the synthesized NNO nanowires.	31
Figure 4.2. XRD patterns for as-spun 0.65PMN-0.35PT nanowires.	32
Figure 4.3. SEM images for the synthesized nanowires as well as commercial nanopowders: (a) NNO nanowires, (b) 0.65PMN-0.35PT nanowires, (c) PZT nanopowders, and (d) BTO nanopowders.	33
Figure 4.4. SEM images of NNO/PVDF nanocomposites with different volume fraction percentages: (a) NNO/PVDF 5%, (b) NNO/PVDF 10%, (c) NNO/PVDF 20%, and (d) NNO/PVDF 30%.	34
Figure 4.5. Digital view of the as-prepared nanocomposites with and without silver paint electrodes: (a) NNO/PVDF and (b) 0.65PMN-0.35PT/PVDF.	35
Figure 4.6. SEM images for nanocomposites containing 0.65PMN-0.35PT and commercial ceramics: (a) 5% 0.65PMN-0.35PT/PVDF, (b) 10% 0.65PMN-0.35PT/PVDF, (c) 30% BTO/PVDF, and (d) 30% PZT/PVDF.	36
Figure 4.7. Dielectric constants for NNO/PVDF nanocomposites as a function of nanowire volume fraction percentages and temperature.	37
Figure 4.8. Dielectric permittivity constants of various nanocomposite capacitors at a temperature of 20°C and a frequency of 1 kHz.	38
Figure 4.9. Dielectric permittivity constants of various nanocomposite capacitors at a temperature of 60°C and a frequency of 1 kHz.	39

Figure 4.10. Dielectric permittivity constant of nanocomposites between a frequency range of 1 kHz-1 MHz at 20°C: (a) NNO/PVDF, (b) PZT/PVDF, (c) BTO/PVDF, and (d) 0.65PMN-0.35PT/PVDF.....	40
Figure 4.11. Dielectric loss at 1 MHz of nanocomposites as a function of filler volume fraction.	41
Figure 4.12. Breakdown strength of NNO/PVDF nanocomposites as a function of nanowires volume fraction percentage and temperature.	42
Figure 4.13. Breakdown strength values of various nanocomposites at 20°C.....	43
Figure 4.14. Breakdown strength values of various nanocomposites at 60°C.....	43
Figure 4.15. Maximum energy density for NNO/PVDF nanocomposites as a function of volume fraction percentage.....	44
Figure 4.16. Maximum energy density of advanced dielectric capacitors as a function of volume fraction percentage at 20°C.....	45
Figure 4.17. Maximum energy density of advanced dielectric capacitors as a function of volume fraction percentage at 60°C.....	46
Figure 4.18: Specific energy for NNO/PVDF nanocomposites as a function of volume fraction.	47
Figure 4.19: Specific energy for nanocomposites as a function of volume fraction at 20°C.	47
Figure 4.20: Specific energy for nanocomposites as a function of volume fraction at 60°C.	48

Chapter 1: Introduction

1.1 OVERVIEW

The development of next generation electrical energy storage devices has gained tremendous attention within the scientific community due to their numerous applications in modern electronics. Several research efforts have been oriented to achieving new series of energy storage devices capable of powering a wide range of electrical products starting from portable electronics such as cell phones, digital cameras, tablets, and laptops, or developing technologies such as hybrid electric vehicles, prosthetic products, pulse power applications, and stationary power systems [1]. The growing need for these applications has demanded significant progress in order to achieve electrical devices displaying higher energy and power densities, as well as elevated rate capabilities.

Among all the energy storage devices, batteries and capacitors represent the two most widely employed mechanisms in modern electronics. Within rechargeable batteries, electrical energy is generated through the conversion of chemical energy via Faradaic reactions. Thus, a series of chemical reactions taking place within the phase boundary of the electrode/electrolyte interface allow the transfer of electrons and charge storage [2]. Conventional capacitors follow a simpler energy conversion process when compared with batteries. Within capacitors, an external electrical field is responsible for generating a deficiency and excess of electron charges between both conductive plates. Therefore, electrical energy is stored as surface charge between both capacitor plates without undergoing chemical changes; this process is known as non-Faradaic reaction [3].

In order to characterize the performance of energy storage devices two main terms must be introduced: energy density and power density. The first term refers to the energy content available for accomplishing a given work and it is usually expressed either as watt-hours per kilogram (Wh/kg) or Joules per cubic centimeters (J/cc). The second term denotes the rate capability of the system and is

commonly expressed as a function of watts per kilogram (W/kg) [2]. A Ragone plot containing the power and energy densities of various energy storage devices is shown in Figure 1.1. Among rechargeable batteries, lithium-ion batteries have displayed energy densities above 100 Wh/kg, while typical values for conventional capacitors lay below 0.1 Wh/kg [4]. Conventional capacitors have displayed the highest power density values, frequently above 5 kW/kg [5]. Besides their significant higher power densities and fast charge/discharge rate, capacitors have also earned their place in modern electronics due to their higher cyclability. Since batteries operate under Faradaic reactions, their numbers of charge and discharge cycles are typically limited to 1,000-10,000 cycles due to certain irreversibilities arising during the oxidation and reduction processes. Due to their non-Faradaic process, capacitors are capable to display longer lifetimes when compared with batteries [3]. Therefore, this research aims to develop a new series of dielectric capacitors capable of displaying current properties combined with enhanced energy density values.

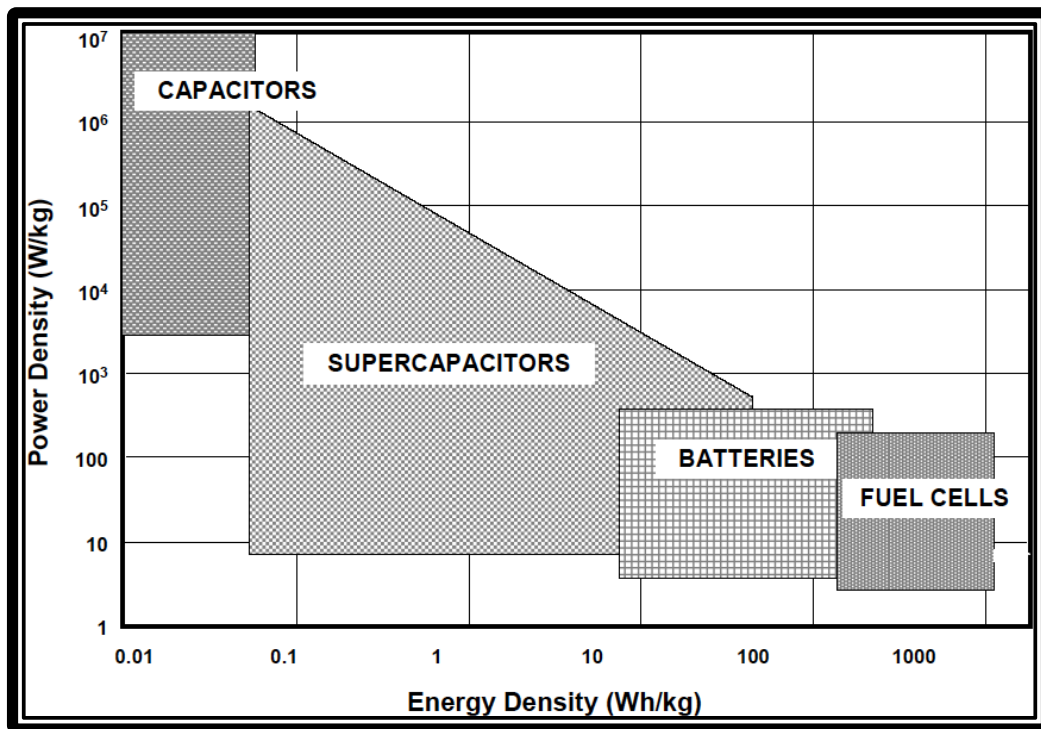


Figure 1.1. Ragone plot of various energy storage devices displaying their power and energy densities [6].

Capacitors are considered an essential component in modern electronics. They operate under the working principle of storing electrical charge inside an insulating material placed between two metallic electrodes. The origin of capacitors goes back to the 1740's when Ewald Georg von Kleist and Pieter van Musschenbroek developed simultaneously and independently a device capable of storing and releasing electrical charge known as the Leyden Jar condenser [7]. In both concepts, Kleist and Musschenbroek employed a narrow-neck glass jar partially filled with water or an aqueous acidic electrolyte in contact with a metal foil electrode attached to the inner wall of the jar. The electrostatic charge was applied to the system through a metal rod electrode inserted throughout the top of the glass jar and attached to the inner metal foil by a metal chain [8]. A digital view and a schematic cross-sectional view of the Leyden jar are shown in Figure 1.2 (a) and Figure 1.2 (b), respectively.

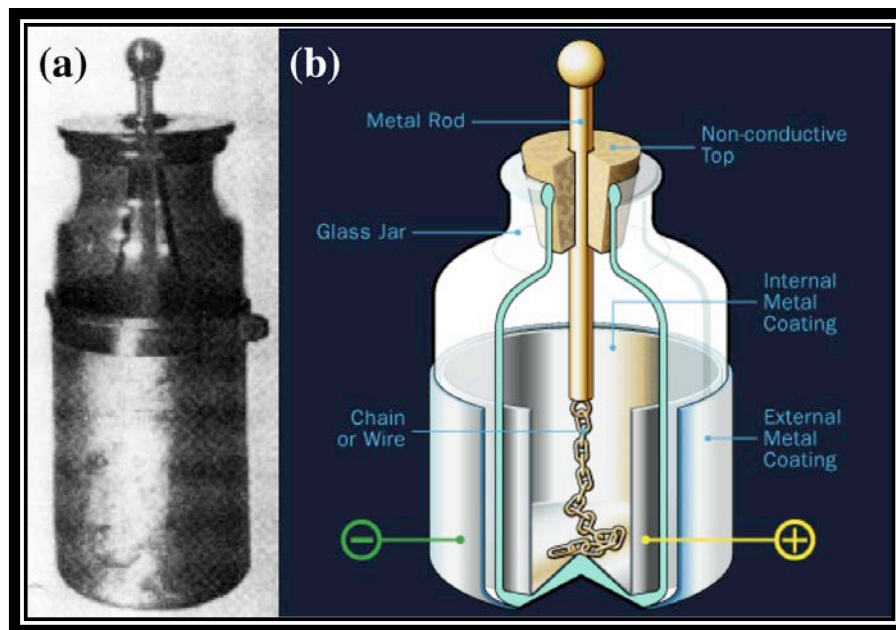


Figure 1.2. The Leyden jar, which is known as the first capacitor in history: (a) digital picture view [3] and (b) schematic cross-section view.

Further modifications to the Leyden jar condenser resulted in the development of the first flat capacitor. During the 1750's, the American inventor Benjamin Franklin determined that the aqueous solution inside the Leyden jar did not represent an essential component for its operation. As a result,

Franklin designed the first flat capacitor employing a piece of glass between two metallic electrodes [9]. Besides Franklin's contribution, Michael Faraday is recognized for developing the first practical capacitors and establishing the initial concepts of dielectric constant, polarization in dielectrics, and electrical force in dielectric materials [3].

Commercial capacitors appeared during the early years of the 20th century. The evolution in the communications industry required the implementation of capacitors into telephones, telegraphs, and radio circuits operating on low voltages [10]. These early capacitors employed wax-impregnated dielectric paper in contact with foil electrodes. The presence of voids within the capacitors due to the solidification of wax was the main factor responsible for failures at elevated voltages [10]. In order to prevent these voids, wax was replaced by petroleum jelly and mineral oil [8]. Later on, impregnated dielectric paper was replaced by mica due to its elevated dielectric constant and remarkable discharge resistance. The implementation of mica as a dielectric material led the development of future generations of capacitors. Further investigations displayed higher quality commercial capacitors such as electrostatic or dielectric, electrolytic, and electrical or electrochemical double-layer capacitors.

As stated before, electrostatic or dielectric capacitors are referred as conventional capacitors and correspond to the first generation of capacitor systems. These energy storage systems accumulate electrical charges within the dielectric material located between two conducting plates without suffering chemical reactions. The second generation of commercial capacitors is represented by electrolytic capacitors. Similar to batteries, electrolytic capacitors employ an electrolyte solution that allows conduction between both, the dielectric and the electrode. These electrolytes either may be solid electrolytes such as manganese oxide (MnO_2) or liquid ones such as sulfuric acid (H_2SO_4). Typical dielectrics employed in electrolytic capacitors include aluminum (Al), tantalum (Ta), or other ceramic insulators [11]. Previous electrolytic capacitors have displayed capacitance values within the range of 0.1 to 10 μF and operation voltages up to 50 V [12].

Due to recent progress in energy storage devices, a third generation of capacitor systems emerged: the electrochemical supercapacitors (ES). Similarly to batteries, ES employs two collecting plates, an electrolyte solution, and a separator. The electrode/electrolyte interface for ES is shown in Figure 1.3. Supercapacitors have also been influenced by Faradaic and non-Faradaic reactions. Therefore, two categories of ES may be found in energy storage applications: electrical and electrochemical double-layer capacitors [6].

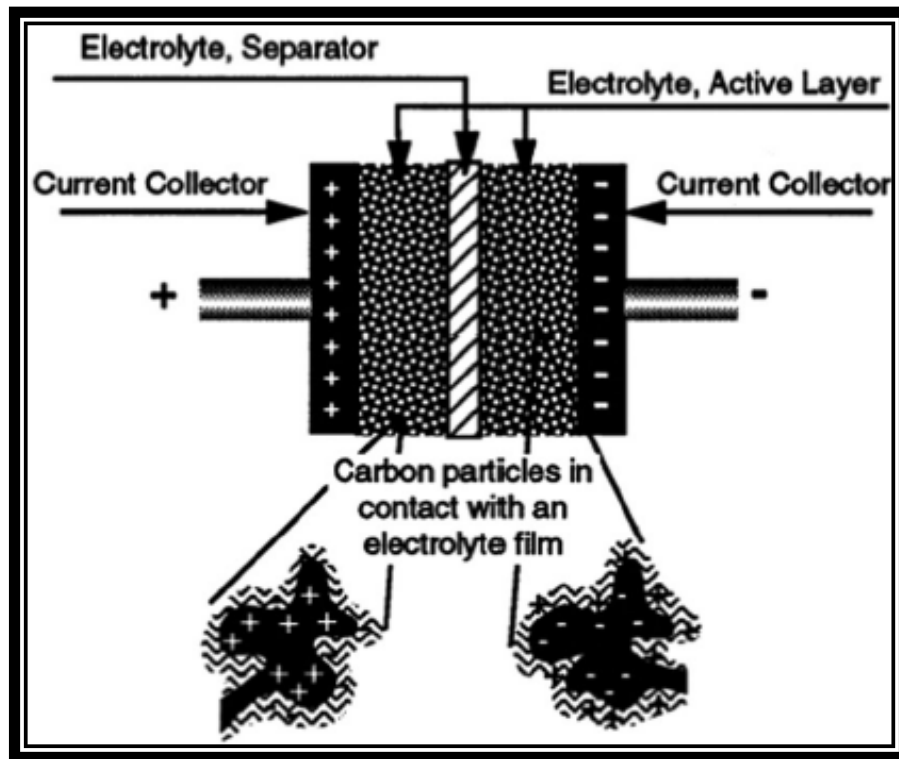


Figure 1.3: Schematic diagram of a single-cell double layer capacitor [13].

The electrical double-layer capacitors, also referred as ultracapacitors, have been referred as physical batteries due to the nature of the non-Faradaic process that includes pure physical charge accumulation [3]. In electrical double-layer capacitors, energy is stored inside the electrode/electrolyte interface due to the accumulation of charges within the electrode surface and the electrolyte ions [13]. In order to increase the efficiency of these capacitor systems, high surface area carbon-based electrodes containing different materials such as carbon aerogels, activated carbon, and carbon nanotubes are

employed [14]. Recent advantages in ultracapacitors have displayed improved energy density values below 10 Wh/kg. Unfortunately their operation voltages ($< 3\text{V}$) are still constrained depending in the type of electrolyte employed [4].

The second group of ES is known as electrochemical double-layer capacitors or pseudocapacitors. Opposite to electrical double-layer capacitors, the electrodes in pseudocapacitors undergo a series of reversible Faradaic reactions whenever they are subjected to an external electrical field. This applied potential generates a sequence of oxidation-reduction and intercalation processes responsible for allowing the free flow of electrical charges between the electrode and electrolyte [15]. Common electrodes employed in pseudocapacitors are made out of metal oxides or conducting polymers. Among metal oxides, ruthenium oxide (RuO_2), cobalt oxide (Co_3O_4), and titanium dioxide (TiO_2) have excelled due to their high capacitance values displayed [11]. Compared with commercial capacitors, pseudocapacitors have been able to achieve higher capacitance values due to an increment in the surface area of the electrodes and a reduction in the thickness of the system. Typical capacitance values for this type of capacitors can be 10-100 higher when compared with ultracapacitors. Current electrochemical double-layer capacitors have been able to combine the energy density of rechargeable batteries and the high power density values of capacitors. Thus, pseudocapacitors have been able to fill the gap between conventional capacitors and pseudocapacitors due to energy density and power density values above 10 Wh/kg and 10 W/kg, respectively [4].

Despite their improved energy storage properties, the implementation of ES in several commercial applications is still limited due to some disadvantages. Current ES have displayed higher energy densities than other dielectric or electrolytic capacitors. Unfortunately, the energy density of rechargeable batteries ($>150\text{ Wh/kg}$) is still significantly higher when compared with those values displayed by ES [5]. Compared with other energy storage devices, ES have also displayed high self-discharging rates. Their implementation in certain applications has been restricted because of short

confinement of energy and self-discharging rates around 10-40% per day [16]. The operation temperature of ES also plays a key factor. Recent ES have exhibited operation temperature ranges between -40 and 70°C [13]. Hence, their implementation in aerospace and defense applications requiring elevated temperatures is still restricted. Finally, the mass production of ES has been limited due to elevated production costs. In addition to the separator and electrolyte costs, the elevated costs of electrode materials represents a challenge for future research efforts. These elevated costs arise from the raw materials and manufacturing procedures. Common carbon-based electrodes employed in ES are found within the market at prices above US\$ 50 [17]. Thus, further investigation may be conducted in order to counteract the current disadvantages of ES and allow their implementation in modern electronics.

Therefore, among the different types of commercial capacitors, dielectric capacitors are still the most commonly used due to its easy processing capability, low cost, high operation voltage, low dielectric loss, and reliability. Previously developed conventional capacitors have exhibited operation voltages within 50 and 400 V and they have yielded capacitance values in the range of 0.1 to 1 μF [11]. A series of important parameters for advanced capacitor systems are summarized in Table 1.1. Besides their high operation voltages, dielectric capacitors have also displayed higher operation temperatures and frequency ranges compared to electrolytic capacitors as shown in Table 1.1. Unfortunately, the energy density values recorded for current conventional capacitors lay below 1 J/cc. Hence, additional research efforts may be implemented in order to develop high energy density dielectric capacitors, in order to take advantage of their operation temperatures ($>100^\circ\text{C}$) in aerospace, defense, and industrial applications among others. Depending on the insulating material employed, conventional dielectric capacitors have been divided into polymer-based and ceramic-based subgroups.

Table 1.1. Operation parameters and energy density values for current advanced capacitor systems [18].

Capacitor System	Energy Density (J/cc)		Operating Temperature (°C)	Operating Frequency
	Now	Future		
Polymer Film	1	10	125	100 kHz
Ceramic	0.1 – 0.5	10	> 200	100 KHz
Electrolyte	1.5 – 2.5	4 – 5	60	100 Hz
Mica	0.2 – 0.5	N/A	> 300	> 1 MHz

Polymer-based dielectric capacitors have found several applications due to their high breakdown strength, low dissipation factor, easy processing capability, high-voltage capabilities, and low weight [19]. A great advantage of polymeric materials is their capability for operating under varying voltages where alternating (AC) and direct (DC) currents are faced. Up to date, there are numerous polymers serving as insulators at a wide range of temperatures and frequencies. Polymer-based capacitors typically can be found in power electronics and pulse power applications. The market for dielectric film capacitors has also been positively impacted due to the development of pulse forming networks (PFNs) employing capacitors for the conversion of electrical energy into the necessary short and fast pulses of energy in the megajoule (MJ) range [20]. However, the performance of polymer-based dielectric capacitors has been limited due to their low dielectric permittivity, which is a parameter responsible for limiting the energy density of a capacitor. A summary of important electrical properties of various polymeric films is shown in Table 1.2. Regardless their high breakdown strength values, typical polymer-based capacitors have displayed one-digit dielectric constants [21]. Among polymer films, polyvinylidene fluoride (PVDF) stands out because of its permittivity constant value around 12 [18]. Therefore, this material may represent a promising alternative for increasing the energy density values of polymer-based capacitors. A digital view as well as a schematic view of commercially available plastic capacitors is shown in Figure 1.4 (a) and Figure 1.4 (b), respectively.

Table 1.2. Common electrical properties of polymer-based capacitors [18].

Polymer Film	Dielectric Permittivity (1 kHz)	Breakdown Strength (MV/m)	Maximum Operation Temperature (°C)
Polycarbonate (PC)	2.8	350	150
Polypropylene (PP)	2.2	500	105
Polyester (PET)	3.3	400	125
Polyvinylidene fluoride (PVDF)	12	200	105
Polyethylene naphthalene (PEN)	3.1	440	137
Polyphenylene sulfide (PPS)	3	360	200

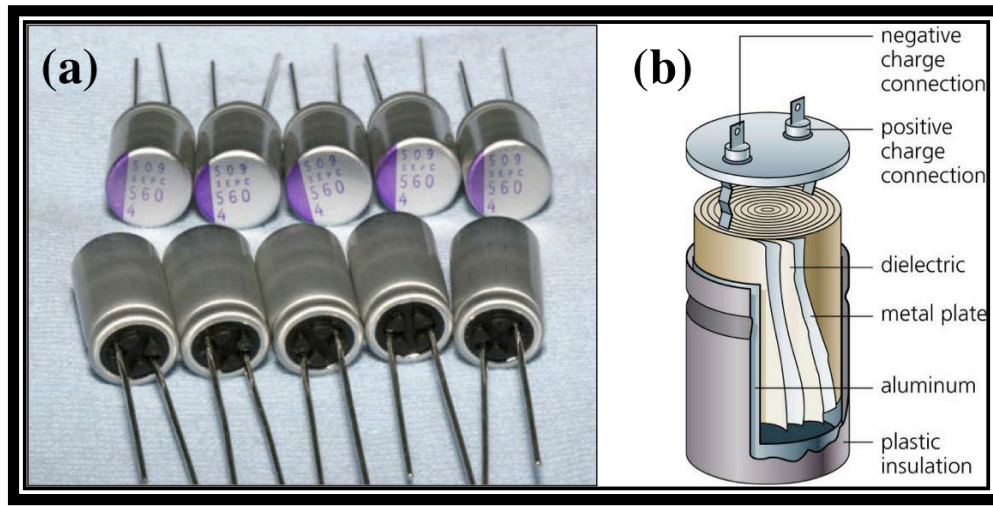


Figure 1.4. Commercial polymer-based dielectric capacitors: (a) digital picture view, and (b) schematic cross-sectional view.

In order to compensate for the low dielectric permittivity values displayed by polymers, ceramic-based capacitors have been implemented. Usually, ceramic capacitors are composed of various layers of dielectric ceramics and metallic electrodes sandwiched between two protective layers. These capacitors are known as multilayer ceramic capacitors (MLC's) and typically display capacitance values around 10 μF [11]. Several research efforts have studied the electrical properties of numerous ceramics such as silicone nitrate (Si_3N_4), silicon oxide (SiO_2), aluminum oxide (Al_2O_3), zinc oxide (ZnO), barium titanate (BaTiO_3), lithium niobate (LiNbO_3), lead zirconia titanate ($\text{Pb}(\text{Zr}_{1-x}\text{Ti}_x)\text{O}_3$), and lead titanate (PbTiO_3). A list of various dielectric ceramics is shown in Table 1.3. Among these dielectric materials, the highest

permittivity values have been displayed by lead-containing ceramics. Recent regulations in the European Union, Asia, and the United States have encouraged the reduction of lead and other heavy metals from electronic equipment due to health and environmental hazards [22]. Therefore, various research efforts have been oriented to developing lead-free dielectric ceramics for modern electronics [23]. Despite their high dielectric constants, the implementation of ceramic-based capacitors at elevated voltage ranges is still limited due to their low breakdown strengths, resulting in lower energy densities. Hence, further modifications in their atomic structure and morphology may result in improved dielectric properties. Moreover, the application of ceramic-based capacitors has also been limited by their brittle nature, which is responsible for affecting their manufacturing process [24]. A digital view as well as a schematic diagram of ceramic-based capacitors is shown in Figure 1.5 (a) and Figure 1.5 (b).

Table 1.3. Dielectric permittivity values for commonly employed engineering ceramics [25].

Perovskite Ceramic	Dielectric Permittivity
Lead Magnesium Niobate-Lead Titanate (PMN-PT)	3,640
Lead Lanthanum Zirconate Titanate (PLZT)	2,590
Barium Titanate (BaTiO_3)	1,700
Potassium Sodium Niobate ($(\text{K}_{0.5}\text{Na}_{0.5})\text{NbO}_3$)	290
Lead Metaniobate (PbNb_2O_6)	225
Sodium Niobate (NaNbO_3)	209
Titanium Dioxide (TiO_2)	80
Hafnium Oxide (HfO_2)	25
Aluminum Oxide (Al_2O_3)	9
Silicon Oxide (SiO_2)	3.9

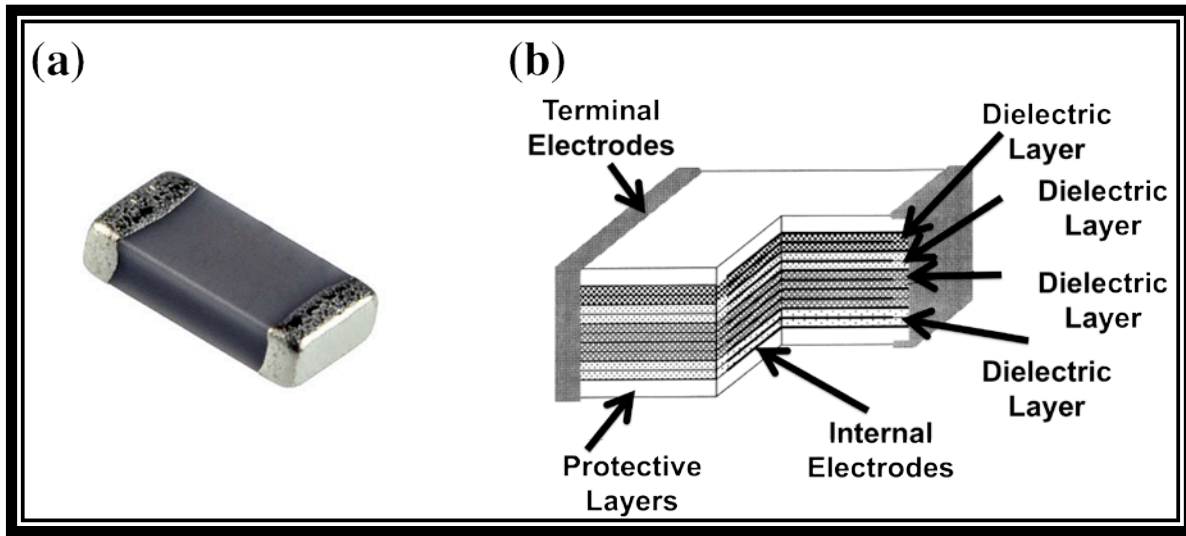


Figure 1.5. Commercial multilayer ceramic capacitors: (a) digital view and (b) schematic cross-sectional view [26].

With the idea of counteracting the disadvantages of polymer-based and ceramic-based dielectric capacitors, a good deal of research efforts have been devoted to combine the high dielectric constant of ceramics and high breakdown strength of polymers inside a single capacitor following the composite approach. Currently, there is wide number of thermoplastics and thermosets available for composite fabrication such as polycarbonate (PC), polyester (PET), epoxy resins, and polyimides (PI). The main benefits of implementing the composite approach are the capability for manipulating and improving determined characteristics such as the electrical, mechanical, and thermal properties of the composites depending on the amount and type of ceramic fillers dispersed within the polymer matrix [27]. Recently, a wide number of fillers in the micro and nano scale have been developed. Among these fillers, nanomaterials have gained tremendous attention due to their remarkable physical and chemical properties when compared to those of bulk materials [28].

Nanotechnology has become a promising field of research thanks to the U.S. National Nanotechnology Initiative (NNI) disclosed in the year 2000. Numerous studies have revealed potential

applications for nanostructures in various brands of electronics, communications, transportation, health, energy, and national security [29]. In order for a material to be considered a nanostructure, it must display at least one dimension within the nanoscale range of 1-100 nm. Depending on their morphology and the number of dimensions not confined to the nanoscale range, nanostructures are classified into four different groups: zero-dimensional (0-D), one-dimensional (1-D), two-dimensional (2-D), and three-dimensional nanostructures (3-D). The major examples of 0-D nanostructures are nanopowders and nanoparticles, while nanowires, nanorods, nanotubes, and nanobelts are a good example of 1-D nanostructures. Thin films and nanocoatings are considered 2-D nanomaterials. Finally, those materials displaying similar nanocrystalline structures and morphologies to 0-D, 1-D, and 2-D nanomaterials and all of their dimensions above 100 nm will be considered as 3-D nanostructures [30]. The remarkable changes in physical and chemical properties of nanomaterials are directly proportional to the increment up to seven orders of magnitude in the surface area and surface energy when compared to particles in the centimeter size [31]. Therefore, dielectric film capacitors containing nanofillers may represent an extraordinary alternative for currently employed dielectric capacitors. Previous synthesized 1-D nanostructures are exhibited in Figure 1.6.

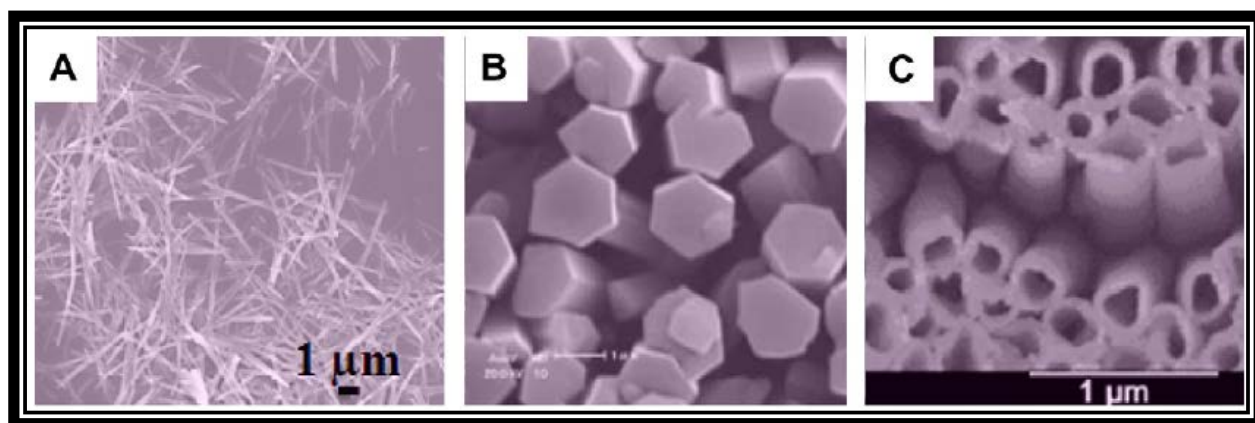


Figure 1.6. Common 1-D nanostructures previously synthesized by several research groups: (a) nanowires, (b) nanorods, and (c) nanotubes [32].

1.2 OBJECTIVE

The main goal of this research is the preparation and characterization of dielectric polymer capacitors reinforced with 1-D ceramic nanofillers. These advanced dielectric capacitors will be delivered through a nanocomposites approach, capable of combining the high dielectric constants and breakdown strengths of ceramic-based and polymer-based capacitors, respectively, in order to achieve enhanced energy storage capabilities. A schematic diagram of the resulting advanced nanocomposite capacitor is shown in Figure 1.7.

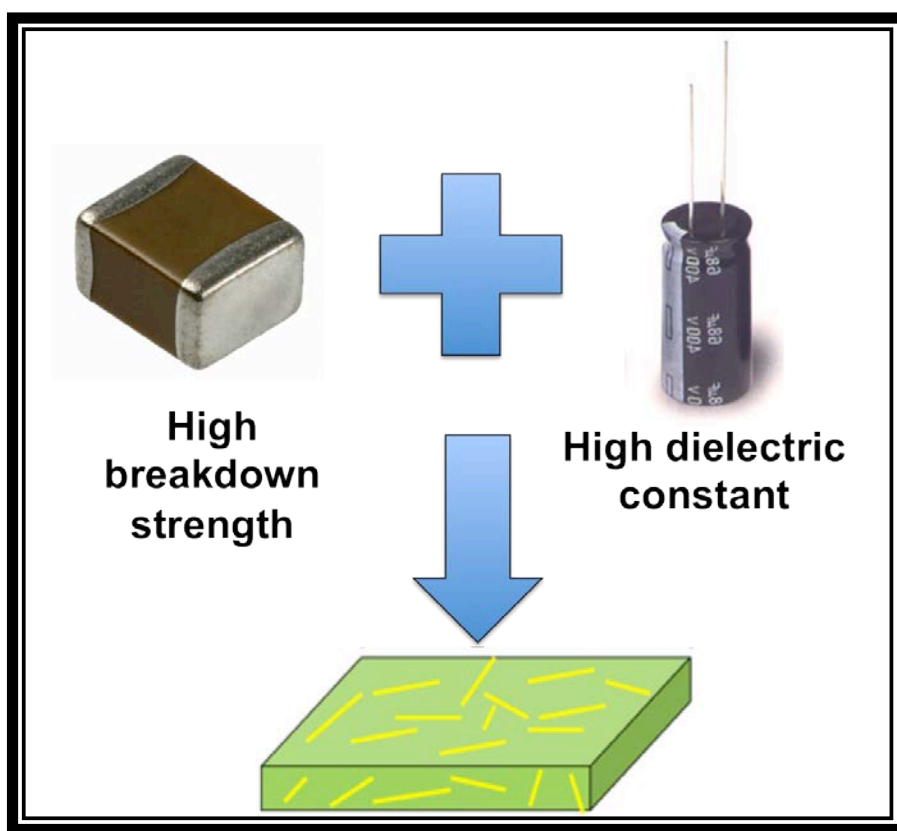


Figure 1.7. Schematic diagram for an advanced nanocomposite capacitor capable combining electrical properties of both polymer and ceramic-based capacitors.

Lead-free sodium niobate (NaNbO_3 or NNO) nanowires and lead-containing lead magnesium niobate-lead titanate ($((1-x)\text{Pb}(\text{Mg}_{1/3}\text{Nb}_{2/3})\text{O}_3-x\text{PbTiO}_3$ or PMN-PT) nanofibers are synthesized following hydrothermal and electrospinning routes, respectively. The morphology and crystal structure of the as-

prepared nanowires are characterized using Scanning Electron Microscopy (SEM) and X-ray diffraction (XRD) analysis. Nanocomposites containing NNO and PMN-PT fillers into a polyvinylidene fluoride (PVDF) matrix are fabricated through a solution casting process. The dielectric constant and breakdown strength of nanocomposites with volume fractions ranging from 5% to 30% are experimentally tested to determine the maximum energy density and specific energy of the nanocomposites. The electrical properties of the as-prepared nanocomposites are also compared with those of commercially available barium titanate (BaTiO_3 or BTO) and lead zirconia titanate ($\text{Pb}(\text{Zr}_{1-x}\text{Ti}_x)\text{O}_3$ or PZT) nanopowders in order to analyze the effect of 1-D nanostructures inside a PVDF matrix and the viability of expelling lead-containing materials from high dielectric applications. Besides the possibility of achieving high energy density dielectric capacitors, this nanocomposite approach also allows the opportunity for developing dielectric capacitors suitable for current and future applications where high temperatures, voltages, and frequency ranges are presented.

Chapter 2: Literature Review

2.1 CAPACITORS

2.1.1 Fundamentals of Capacitors

Capacitors represent an essential component of modern electronics due to their capability of accomplishing two vital tasks. These devices are capable of storing electric charges and assisting with filtering duties whenever certain frequencies are required inside an electrical circuit. The main components of a capacitor are the two metal electrodes allowing the free flow of electrons, as well as the dielectric material placed between them. When a voltage is applied to a capacitor, energy is stored inside the dielectric positioned between the two conductive plates following a non-Faradic process; electrical charges are deposited in an electrostatic manner directly on the plates of the capacitor without suffering chemical changes [3]. Whenever filtering tasks are required inside an electronic device, capacitors are capable to eliminate undesired frequencies and prevent the flow of direct current (DC) within the systems [11]. A schematic presentation of an electrostatic capacitor is shown in Figure 2.1.

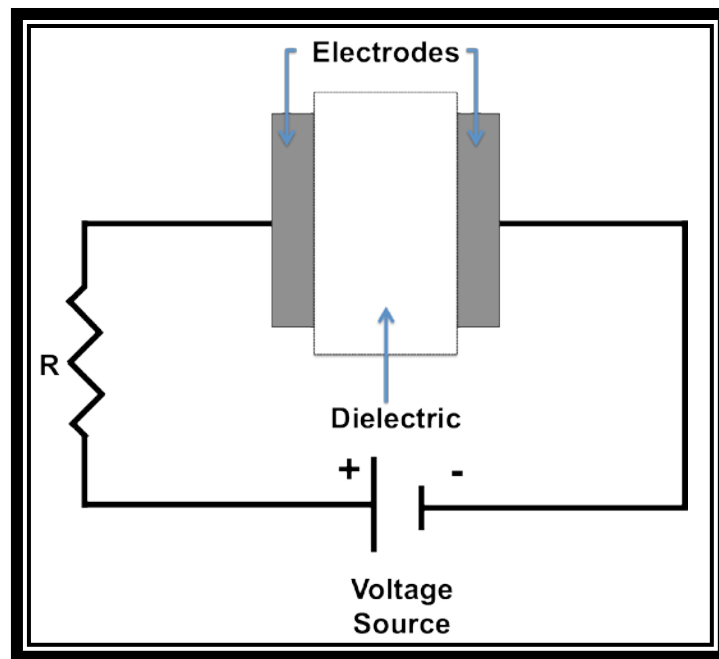


Figure 2.1. Schematic presentation of the main components of an electrostatic capacitor.

In order to understand the performance of a capacitor, the following important concepts must be outlined: capacitance (C), dielectric constant (ϵ_r)

enhancing their dielectric, piezoelectric, and electromechanical properties, allowing their application in numerous electronic devices [33]. Perovskite oxides exhibit a chemical composition of the ABO_3 form and are ideally represented by a cubic closed-packed structure consisting of a B cation in the unit cell's center, oxygen ions stacked in the middle of each one of the six faces of the cubic structure, and finally A cation in the corners of the cube [22]. The ideal perovskite structure is represented in Figure 2.2. Frequently employed A-site large cations are Pb^{2+} , Ba^{2+} , Bi^{3+} and Sr^{2+} , while Mg^{2+} , Zn^{2+} , Ti^{4+} , and Na^{5+} represent the most common B-site small cations [34].

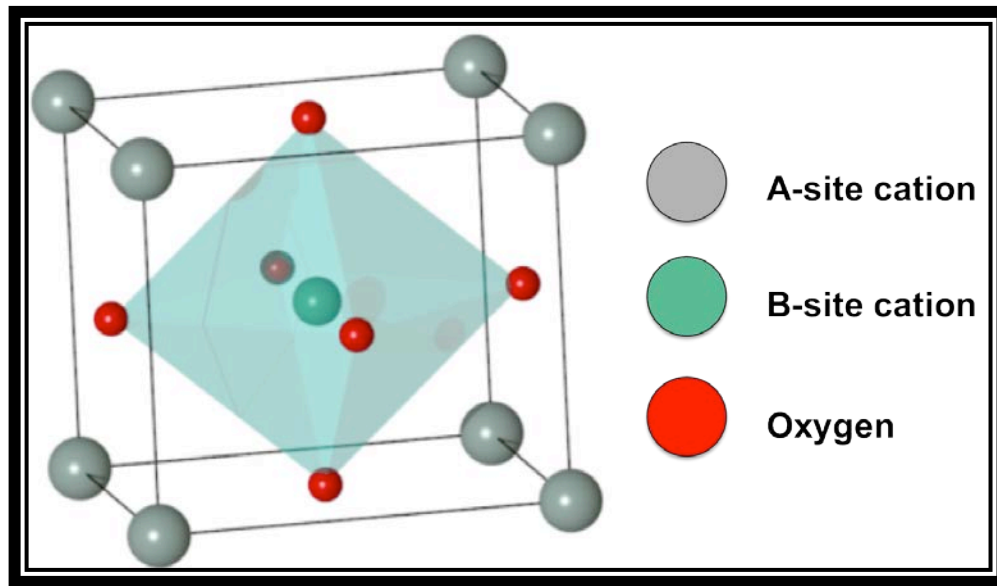


Figure 2.2. The ideal perovskite cubic closed-packed unit cell [22].

Perovskite structures are found in different crystal systems. This is mainly due to their capability for adapting to a series of discrepancies between the length of the A-O and B-O bonds [35]. The crystal symmetry of a perovskite material might be predicted through the calculation of Goldschmidt tolerance factor. If an ideal perovskite model is represented by perfect spherical ions, the tolerance factor (t) may be calculated by the following equation:

where R_A , R_B , and R_O represent the radii for A cation, B cation, and oxygen, respectively [33]. Perovskites displaying $t < 0.95$ exhibit either rhombohedral or orthorhombic structures, composites in the range of $0.95 < t < 1$ display cubic structures, while materials with $t > 1$ show cubic or tetragonal crystal symmetries [36]. The tolerance factor of a perovskite structure plays a key role in the performance of the material. Compounds with a tolerance factor within $0.90 < t < 1.1$ demonstrate a stable behavior, while $t > 1.1$ values are responsible for preventing crystallization of compounds, affecting its dielectric and piezoelectric properties [22].

Perovskite ceramics have found several applications due to their outstanding electrical and electromechanical properties. A wide number of these perovskite structures demonstrate a permanent and reversible polarization state, known as ferroelectricity. A tremendous advantage of ferroelectric materials is their capability for displaying pyroelectric and piezoelectric behaviors. A pyroelectric material is denoted by its relationship between the electric polarizability and temperature and its ability of producing a momentary voltage in response to temperature. In pyroelectrics, atoms are rearranged within the crystal structure due to a change in temperature, resulting in a change in polarization [37]. Piezoelectric materials are capable of generating a voltage in response to applied mechanical strain. The reverse piezoelectric effect is also displayed in these perovskite structures and it's denoted as the mechanical force generated in response to an applied electrical field [21]. The main condition responsible for these outstanding properties exhibited by piezoelectric ceramics lays in their absence of a center of symmetry, which is responsible for the development of this remarkable dielectric polarization. As a result of their polarizability, perovskite ceramics exhibit higher permittivity constants and electromechanical coupling coefficients when compared to other engineering ceramics.

2.3 SYNTHESIS OF 1-D NANOSTRUCTURES

The preparation of nanomaterials has been reached through the implementation of two different approaches: top-down and bottom-up. The top-down method is characterized by the employment of physical techniques such as lithography, milling, etching, electron-beam, and focused-ion beam. Because of these physical procedures, 1-D nanostructures are reached after downsize of larger structures [38]. Unfortunately, nanomaterials produced through the top-down approach have displayed a series of crystallographic damages, impurities, and surface imperfections due to the nature of these techniques and the presence of internal stresses [39]. These defects have a significant impact on the chemical and physical properties of the nanomaterials, reducing various properties such as their conductivity and mechanical properties [31]. The growth of 1-D nanostructures has also been achieved by the implementation of the bottom-up approach. This method employs a variety of chemical procedures in order to assemble nanomaterials from individual components: atom-by-atom or molecular-by-molecular. Among all the bottom-up technologies available, chemical vapor deposition (CVD), sol-gel processing, electrospinning, vapor (or solution)-liquid-solid (VLS or SLS) method, and hydrothermal or solvothermal reactions represent the most commonly employed growing techniques. Depending on the synthetic route employed, materials may display different crystallinity, chemical compositions, physical properties, and microstructure due to the kinetics involved during these reactions [31]. Compared to the top-down approach, the bottom-up method represents a better alternative for developing nanomaterials in terms of material diversity, cost, and potential for large-scale production [40]. Another important factor for comparing both approaches is the quality of the resulting materials. 1-D nanostructures achieved by bottom-up techniques have displayed more homogeneous compositions as well as a significant reduction in impurities and defects when compared to top-down materials. This is mainly due because of the nature of the bottom-up approach, where reactions are driven by the reduction of Gibbs free energy, resulting in nanostructures reaching a thermodynamic equilibrium state [31,41].

2.3.1 Hydrothermal Method

The hydrothermal method represents a straightforward and relatively simple mechanism for the synthesis of nanocrystalline inorganic materials. The British geologist Sir Roderick Murchison first introduced the term hydrothermal during the 19th Century in order to represent the behavior of water at elevated temperatures and pressures. According to Byrappa et al., a hydrothermal reaction is defined as “any heterogeneous or homogeneous chemical reaction in the presence of an aqueous solvent above room temperature and pressure greater than 1 atm in a closed system” [42]. This technique involves the crystallization and growth of a material starting from a series of precursors or nutrients being exposed to temperature and pressure ranges above ambient conditions [43].

During hydrothermal growth, chemicals are kept inside a pressure vessel known as autoclave or reactor chamber, which is capable of resisting high temperatures and pressures for extended periods. Typically, these reactors are made of stainless steel and they contain an inner lining made out of Teflon. This synthetic method usually takes part in environments with a controlled temperature range between 100 and 300°C, pressures above atmospheric, and reaction periods between 4-24 hours [44]. During hydrothermal reactions, the pressure within the autoclave is a function of reaction's temperature and the amount of chemicals employed [45]. The temperature-pressure relation at constant volumes plays an important role in these reactions, since higher pressure ranges prevent solution evaporation and increase solubility, resulting in more efficient and outstanding synthetic processes [44]. Crystal growth takes place due to the presence of a temperature gradient maintained at the two ends of the autoclave. The hotter area, known as the nutrient zone, dissolves the solution, while the cooler area, referred as growth zone, is responsible for the growth of materials [29,46].

Compared to other synthetic methods, the hydrothermal approach has displayed a wide number of advantages. Through these reactions, it is feasible to prepare complex materials with high crystallinity levels and controlled morphologies. This technique also provides a simple, cost effective,

contamination free, and energy saving synthetic method that facilitates the formation of controlled shapes and dimensions employing lower viscosities and easy mass transportation at lower temperatures [47]. The disadvantages for employing hydrothermal growth are the elevated costs for the autoclaves and the longer reaction periods when compared to other approaches such as CVD, VSL, or milling [29].

Previously, a wide number of ceramic nanowires have been synthesized following hydrothermal route. Metal oxide materials such as titanium dioxide (TiO_2) nanowires have been studied for their application in lithium-ion batteries [48-50]. These materials have displayed diameters between 10 and 100 nm and lengths up to several micrometers. Various perovskite structures have also been manufactured through this technique. Joshi et al. have previously synthesized BaTiO_3 and SrTiO_3 nanowires with diameters between 50-200 nm [51]. LiNbO_3 and KNbO_3 nanowires have also been developed following this growing method [52,53]. Shi et al. developed NaNbO_3 nanowires with diameters of 100 nm using a surfactant-assisted hydrothermal procedure [54]. PMN-PT nanowires with diameters between the range of 200-800 nm and a length up to 40 μm were recently prepared by Xu et al. [55].

2.3.2 Sol-Gel Processing

The origins of sol-gel techniques go back to the 19th Century when Ebelman, Faraday, and Graham synthesized the first silica and gold sols [56]. This method allows the formation of homogeneous, transparent, and amorphous solutions. The sol-gel processing has been suitable for the preparation of organic, inorganic, and organic-inorganic materials [57]. Before describing the reactions involved in this synthetic route, two main terms must be defined: sol and gel. Sols are defined as stable liquid solutions containing a series of solid particles. These particles are known as colloids, they display dimensions of 1-1000 nm and are denser than the surrounding solution. A gel is a porous, interconnected rigid network of colloidal or sub-colloidal materials that expand through a liquid medium [56,58]. During this synthetic method, precursors are mixed through hydrolysis and condensation

polymerization. The resulting ceramic sol-gels are employed to prepare different materials such as powders, fibers, thin films or coatings [59]. Recently, the sol-gel approach has been followed for preparing a series of PMN-PT thin films or even nanoparticles. Calzada et al. study the effect of various annealing temperatures on 0.7PMN-0.3PT sol-gels [60,61]. PMN-PT nanoparticles and nanofibers with dimensions below 100 nm have been synthesized using sol-gels as precursors [62,63].

2.4 NANOCOMPOSITES

Composite materials are constituted of two or more materials owning different properties. These constituent materials are commonly referred as matrix and reinforcement. The matrix material provides support and housing for the reinforcement material, which is typically employed for enhancing the mechanical and physical properties of the matrix. Therefore, composites will exhibit different properties when compared to individual constituent materials [65]. A nanocomposite is defined as a composite material where either the matrix or reinforcement display dimensions in the nano scale. Depending in the constituent materials, nanocomposites are divided into polymer, ceramic, and metal matrix nanocomposites [27].

Recently various research efforts have been devoted to combine the high dielectric constant of ceramics and high breakdown strength polymers employing the composite approach. To date, many research groups increased the energy density of dielectric capacitors using a nanocomposite approach, including: BaTiO₃ nano particles reinforced polycarbonate (PC) [66], poly(vinylidene fluoride-co-hexafluoropropylene) (PVDF-HFP) [67], modified BaTiO₃ nanoparticles with PVDF [68,69], TiO₂ nanoparticles with PVDF terpolymer [70], calcium copper titanate (CCT) reinforced polyimide [71], silver nanoparticle/poly(vinyl pyrrolidone) core-shell structure for high dielectric constant and low loss epoxy matrix composite [72], and PZT and PLZT powders reinforced PVDF [73].

Chapter 3: Methodology

3.1 SYNTHESIS OF NANOWIRES

3.1.1 Synthesis of NaNbO₃ Nanowires

Sodium niobite nanowires were synthesized through a hydrothermal process based in a previously developed method [73]. Initially, a 12 M NaOH solution was prepared by dissolving 33.6 g of NaOH (Acros Organics, 98%) into 70 mL of deionized (DI) water under manual stirring for a period of 15 minutes. Subsequently, 3.5 g of Nb₂O₅ (Aldrich, 99.99%) were added into the NaOH solution. After being stirred for a period of 30 minutes at room temperature, the mixture was transferred into a 160 mL Teflon lined stainless steel autoclave with a fill factor of 80%. The autoclave was placed inside an electrical oven to undergo hydrothermal reaction at 180°C for 4 h. After cooling down to room temperature, white precipitate was filtered, washed with DI water for several times, and dried at 80°C for 12 h. Finally, NNO powders were annealed at 550°C for a period of 4 h in order to achieve well crystallized NNO nanowires.

3.1.2 SYNTHESIS OF PMN-PT NANOWIRES

3.1.2.1 PMN & PT Sols Preparation

In order to obtain an air-stable PMN-PT sol, single PMN and PT sols were synthesized following a diol-based chemical procedure similar to the one reported by Calzada [61]. The synthesis of PMN sol involved a 3-step procedure. First, 2.496 g of Nb₂(OCH₂CH₃)₅ (Aldrich, 99.95%) and 0.449 g of Mg(OC₂H₅)₂ (Aldrich, 98%) were mixed with 2.981 g of HO(CH₂)₃OH (Aldrich, 98%) and 0.336 g of CH₃COOH (Fisher BioReagents, Glacial) inside a 25 mL flask. This solution was first refluxed and then distilled, both times under a nitrogen atmosphere at 120°C for 8 h and vigorous stirring. For the second step, a separate 25 mL flask was filled with 9.399 g of HO(CH₂)₃OH (Aldrich, 98%) and 4.686 g of Pb(C₂H₃O₂)₂·3H₂O (Fisher Chemical, 99-103%). This solution was first refluxed at 130°C for 1 h under

a nitrogen atmosphere and vigorous stirring. Then, the lead-containing solution was distilled at 130°C for 6 h under a nitrogen atmosphere and vigorous stirring. Finally, the lead-containing solution was dispersed dropwise into the Nb/Mg-containing solution and mixed at room temperature for a period of 1 h under vigorous stirring and open atmosphere in order to obtain a gold-transparent solution.

PT sol was synthesized by dissolving 3.489 g of $\text{Pb}(\text{C}_2\text{H}_3\text{O}_2)_2 \cdot 3\text{H}_2\text{O}$ (Fisher Chemical, 99-103%) into 3.044 g of $\text{HO}(\text{CH}_2)_3\text{OH}$ (Aldrich, 98%) via reflux at 130°C for 1 h under a nitrogen atmosphere and vigorous stirring. Right after the reflux, 2.914 g of $[(\text{CH}_3)_2\text{CHO}]_2\text{Ti}(\text{C}_5\text{H}_7\text{O}_2)_2$ (Aldrich, 78 wt.%) were added into the lead-containing solution. This mixture was refluxed at 120°C for 8 h under a nitrogen atmosphere and vigorous stirring. Finally, an orange-transparent and air-stable PT sol was obtained right after the distillation of byproducts at 120°C for 8 h.

Finally, PMN and PT sol were combined in order to obtain a precipitate-free and air-stable PMN-PT sol-gel. In a typical reaction, 8.209 g of PMN sol were mixed with 3.1044 g of PT sol inside a 25 mL flask for a period of 1 h at room temperature and under vigorous stirring. PT sol was added dropwise into PMN in order to prevent precipitations. The resultant sol-gel displayed a nominal composition of $0.65\text{Pb}(\text{Mg}_{1/3}\text{Nb}_{2/3})\text{O}_3$ - 0.35PbTiO_3 and a gold-transparent color.

3.1.2.2 Fabrication of PMN-PT Nanowires Via Electrospinning

0.65PMN-0.35PT nanofibers were acquired through an electrospinning setup following similar parameters to the ones previously mentioned in literature [63]. Prior to the electrospinning, a polymer-containing solution was prepared for increasing the viscosity of the samples and allowing the formation of nanofibers. The employed chemicals for the electrospinning were 0.65PMN-0.35PT sol, polyvinylpyrrolidone (PVP) (Acros Organics, $M_w \sim 1,300,000$) and ethanol. Initially, 0.5 g of PVP were mixed with 7.5 g of ethanol inside a 25 mL glass beaker. This mixture was sited inside a 150 mL glass beaker filled with silicon oil, placed over a hot plate, and heated up at 80°C for a period of 15 min

in order to allow the formation of a clear-transparent homogeneous solution. Once the reaction cooled down, extra ethanol was dispersed into the solution in order to compensate for ethanol losses during the previous step and again heated up at 80°C for 15 min. Then, extra ethanol was added into the mixture to compensate for the amount of evaporated ethanol during the reaction and achieve a solution containing 7.5 g of ethanol. Finally, 2 g of PMN-PT sol were dispersed into the PVP/ethanol mixture under vigorous stirring for a period of 30 min in order to obtain a gold-transparent solution with 20 wt.% 0.65PMN-0.35PT and 5 wt.% PVP content.

A schematic diagram of the electrospinning setup designed for this research is shown Figure 3.1. The 0.65PMN-0.35PT/PVP/ethanol solution was loaded into a 10 mL glass syringe and pumped at a flow of 25 μ L/min using a digitally controlled infusion pump (Harvard Apparatus 22 Digital Syringe Pump). A high voltage power supply (Acopian PO3HP2) delivered a 15 kV voltage suitable for the formation of a stable Taylor cone, which is responsible for the formation of high-quality fibers. The positive electrode of this power source was attached to the syringe's needle while the negative one was connected to the collecting substrate. Silicone wafers were utilized as the collecting plate for these nanofibers. The distance between the needle and the collecting substrate was set to 15 cm, an appropriate distance for the formation of nanofibers with a small diameter. In order to prevent the agglomeration of solution and the formation of 2-D thin films due to the humidity of the solution, a heat source with a temperature output of 150°C was employed during the electrospinning. Figure 3.2 shows an schematic diagram with the location of the heat source. As long as the 0.65PMN-0.35PT/PVP/ethanol solution was pumped through the needle, a white layer of nanofibers with a significant thickness was visible over the collecting plate wall. The substrate plate containing the nanofibers was dried at ambient temperature overnight and then transferred into a high temperature furnace to undergo crystallization process at 600°C for 1 h. Due to its elevated melting point ($>1000^{\circ}\text{C}$), silicon wafers were employed as

collecting substrates in order to facilitate the annealing process. Finally, a razor blade was employed to remove the 0.65PMN-0.35PT nanofibers from the collecting plate.

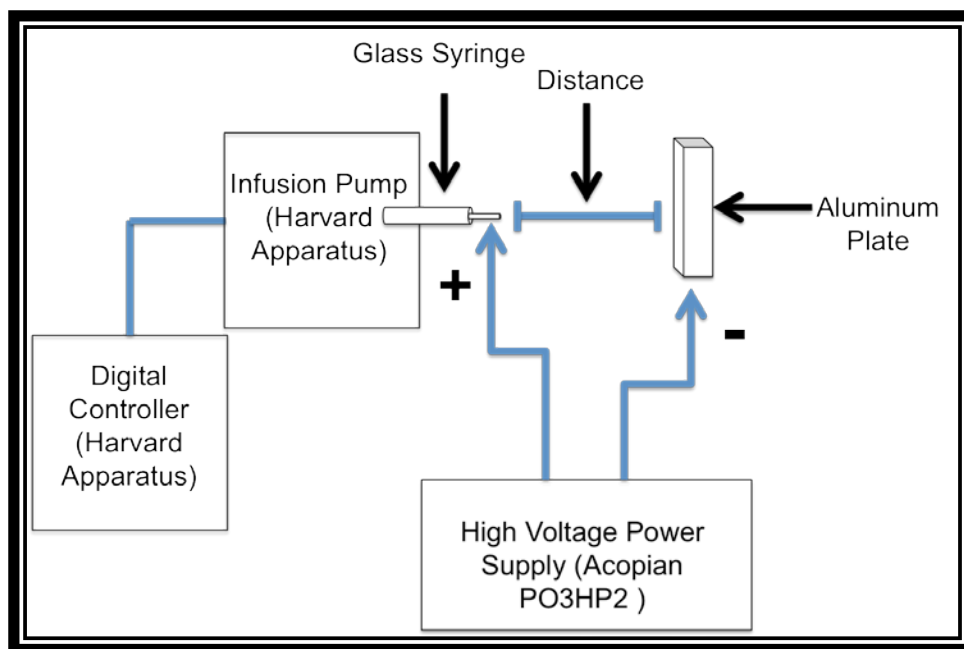


Figure 3.1. Schematic diagram for the developed electrospinning setup.

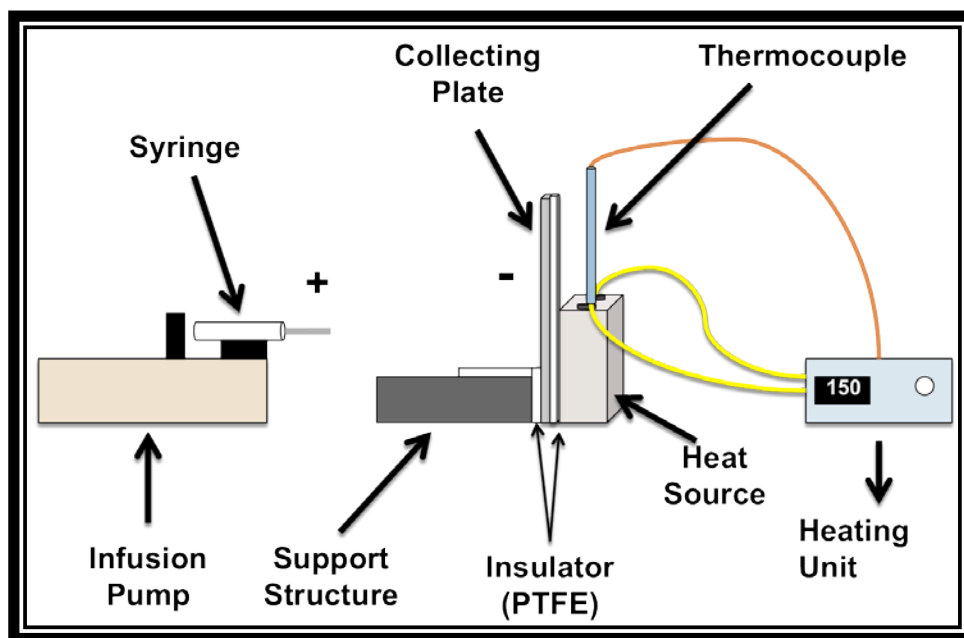


Figure 3.2. Schematic diagram showing the location of the heat source employed during the electrospinning.

3.2 PREPARATION OF NANOCOMPOSITES

3.2.1 NaNbO₃/PVDF and 0.65PMN-0.35PT/PVDF Nanocomposites

Nanocomposites were prepared by dispersing NNO and 0.65PMN-0.35PT nanowires inside a polymer matrix (PVDF/DMF) solution. Initially, PVDF (Aldrich, Mw~53,4000) and DMF (Acros Organics, 99.8%) were mixed at a 1:10 weight ratio and heated up at 80°C for 30 min to fully dissolve the PVDF. The as-prepared nanowires and the PVDF/DMF solution were mixed inside a 25 mL glass beaker by manual stirring, horn sonication (Branson S-450A), and bath sonication (Branson 2510) for several times until a homogeneous mixture was obtained. Subsequently, solution was casted onto a PTFE film and dried at 80 °C for 6 h. In order to achieve a consistent thickness over the entire film, nanocomposites were hot pressed at 160°C for 15 minutes under a constant pressure of 1 ton (Carver, 3850). Finally, top and bottom surfaces of nanocomposites were coated with silver paint as electrodes for electrical testing. The fabrication process of the dielectric film nanocomposites is schematically shown in Figure 3.3.

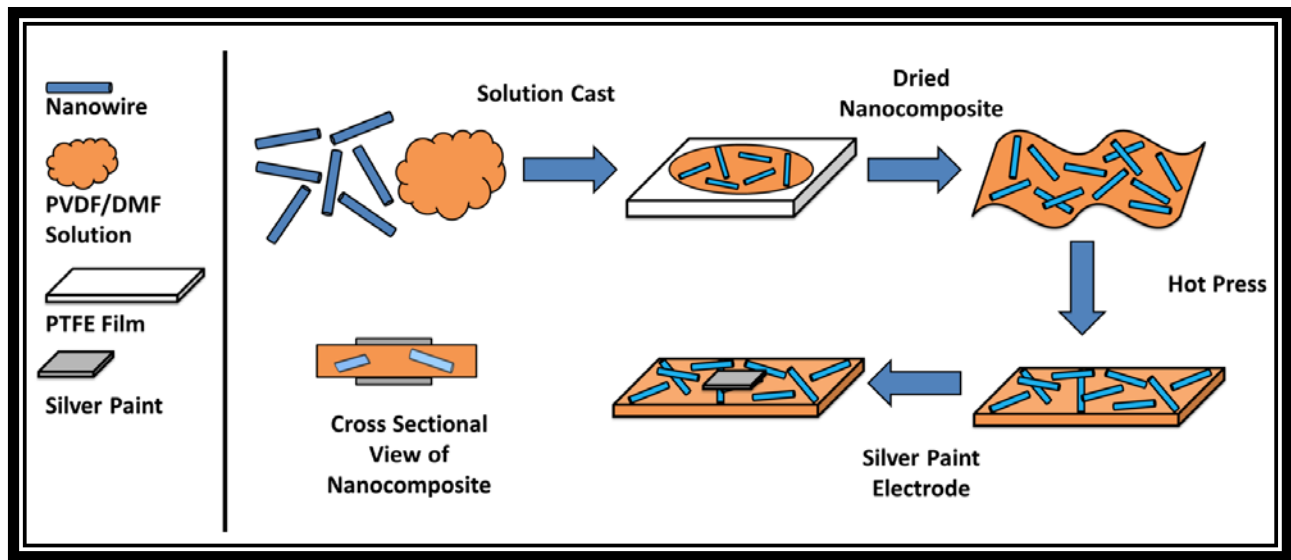


Figure 3.3. Schematic diagram of the manufacturing process of NaNbO₃/PVDF nanocomposites.

3.3 SAMPLES CHARACTERIZATION

The as-prepared NaNbO_3 and PMN-PT nanowires as well as the nanocomposites were characterized through Scanning Electron Microscopy (SEM) and X-ray diffraction (XRD) analysis. Morphological aspects such as shape, length, and diameter of the samples were inspected using Hitachi S-4800 SEM. The crystal structure and the lattice parameters of the nanowires were evaluated through Bruker B8 Discover XRD using $\text{Cu K}\alpha$ radiation at room temperature. The SEM and XRD facilities are shown in Figure 3.4.

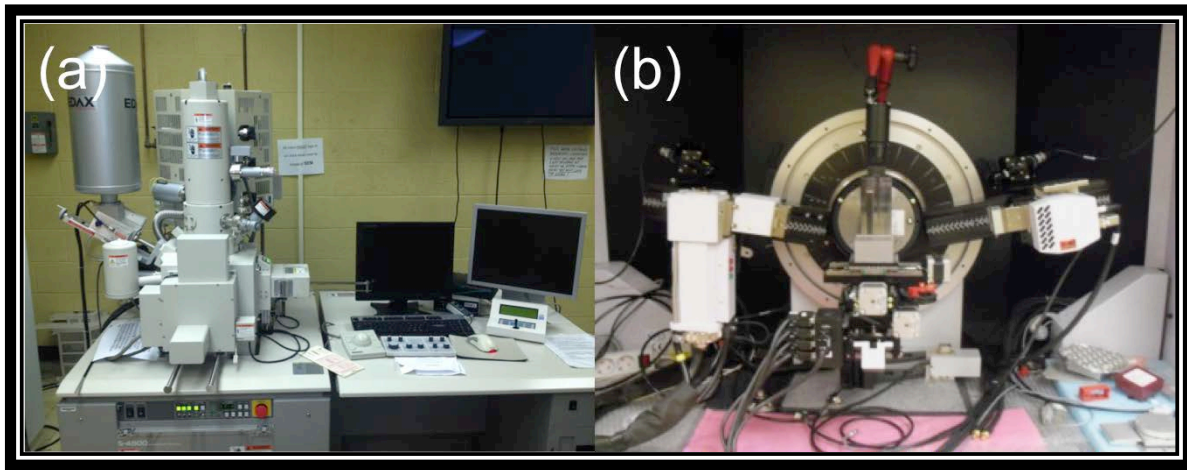


Figure 3.4. Sample characterization facilities available at the University of Texas at El Paso: (a) SEM and (b) XRD.

3.4 ELECTRICAL TESTING

3.4.1 Frequency Dependent Capacitance and Dielectric Loss Tangent

Frequency dependent capacitance and dielectric loss tangent of the nanocomposites were measured using HP 4284A LCR meter within a frequency range between 1 kHz and 1 MHz at 1 Vrms with a parallel equivalent circuit. Figure 3.5 displays the schematic diagram for this analysis. $\text{NaNbO}_3/\text{PVDF}$ and PMN-PT/PI nanocomposites were held inside a 150 mL glass beaker filled with silicon oil in order to study the influence of temperature in capacitance. Nanocomposites were evaluated at the following temperature: 25, 40, 60, and 80°C.

In order to acquire a confident statistical analysis, a total of 5 samples for each different volume fraction nanocomposites were analyzed.

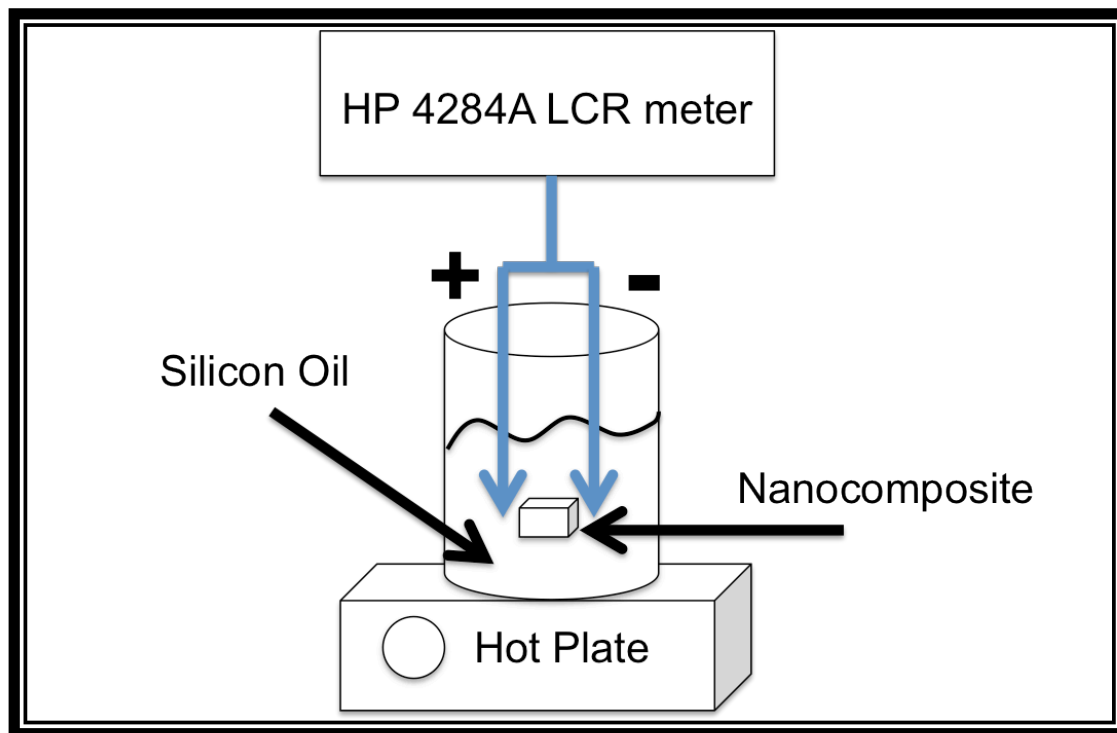


Figure 3.5. Schematic diagram for the frequency dependent capacitance testing.

3.4.2 Breakdown Strength

The breakdown voltages were measured according to the ASTM D149-09 standard [74]. Experimental setup utilized a 30 kV high voltage power supply (Acopian PO3HP2) and a digital oscilloscope (Rigol DS1102E), both connected to a 20 MHz function/arbitrary waveform generator (Agilent 33220A). In order to avoid arcing prior to breakdown, nanocomposites were held inside a 500 mL beaker filled with silicon oil. Breakdown voltage was recorded through a digital multimeter (Danetz BMI DrantTech TRMS System PRO Multimeter) connected to the high voltage power supply. The breakdown strength for each nanocomposites was tested at 25, 40, 60, and 80°C. A schematic diagram for the dielectric strength testing is shown in Figure 3.6.

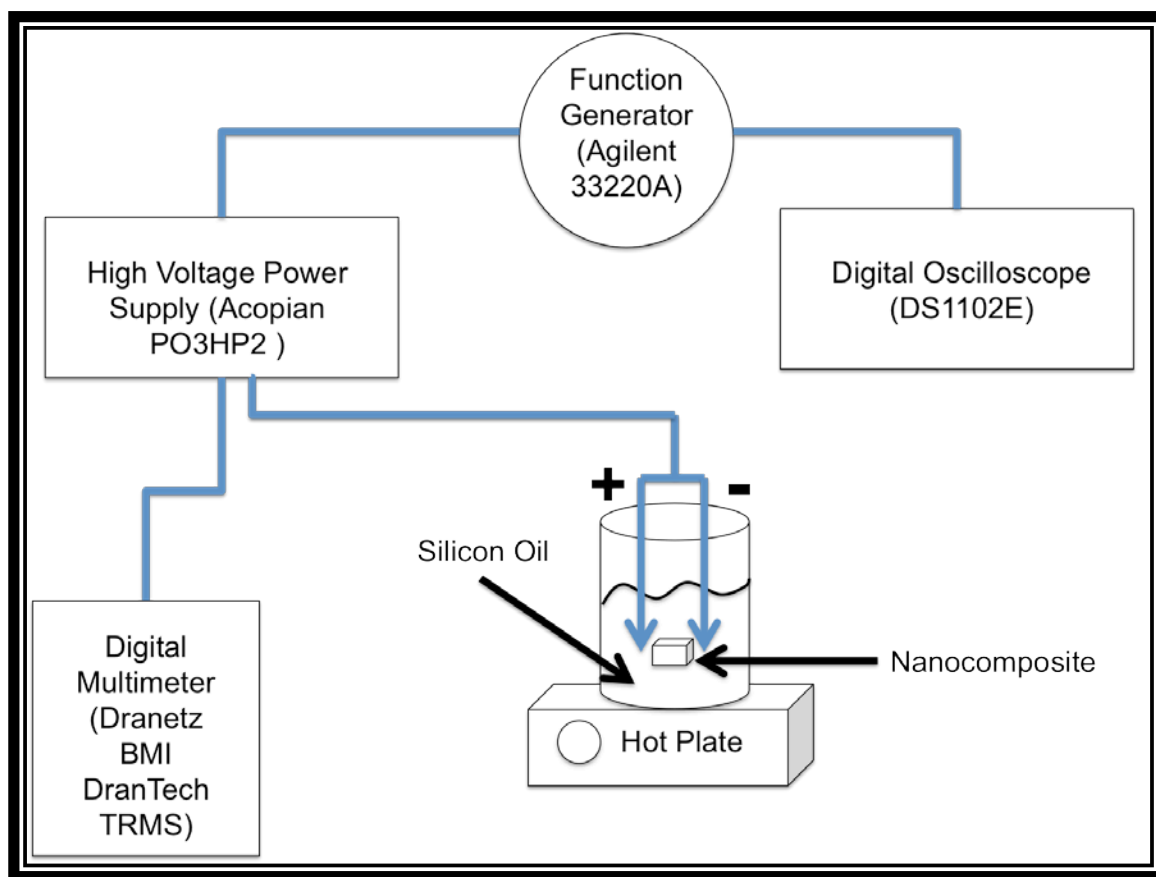


Figure 3.6. Schematic diagram for the breakdown strength testing setup.

Chapter 4: Results and Discussion

4.1 SAMPLE CHARACTERIZATION

4.1.1. Crystal Structure

The resulting crystal structures for the as-prepared nanowires were determined through XRD analysis using Cu K α radiation. The XRD peaks for NNO nanowires are shown in Figure 4.1. Initially, lead-free nanowires revealed an undefined crystal structure hinting a phase transition into sodium niobate. Therefore, nanowires were exposed to a heat treatment at 550°C for a period of 4 hours. Right after the annealing process, the resulting nanowires displayed no other peaks than NNO and revealed an orthorhombic phase with excellent crystallinity. The calculated lattice parameters for these lead-free NNO nanowires are $a = 5.5625 \text{ \AA}$, $b = 15.5495 \text{ \AA}$, and $c = 5.5135 \text{ \AA}$, which are similar values to the ones previously reported on literature [54,75]. The NNO diffraction peaks match exactly with those indicated by the standard card JPCDS of NNO (no. 01-072-7753).

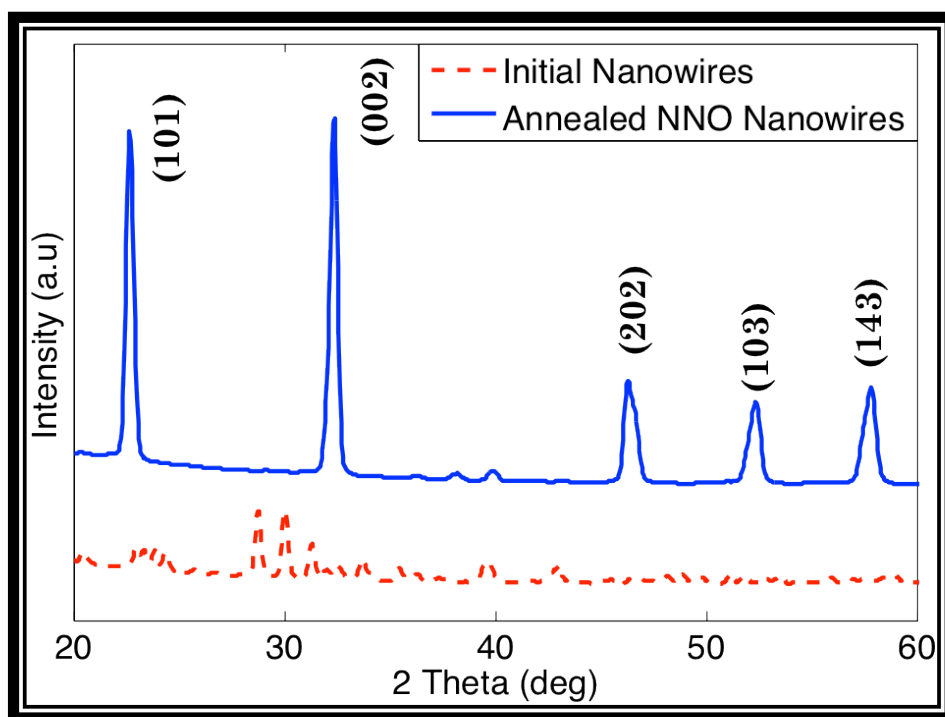


Figure 4.1. XRD patterns for the synthesized NNO nanowires.

The as-spun 0.65PMN-0.35PT nanowires were annealed at 600°C for a period of 1 hour in order to achieve a perovskite crystal structure. The resulting XRD peaks for the lead-containing nanowires are presented in Figure 4.2. These 0.65PMN-0.35PT nanowires displayed a cubic structure with lattice parameters $a = b = c = 4.0387 \text{ \AA}$. Regardless the annealing process, 0.65PMN-0.35PT nanowires displayed a crystal structure combining the main peaks for perovskite structure complemented by many pyrochlore peaks. Previously, it has been documented in literature that niobium-containing compounds demonstrate a phase transformation from pyrochlore to perovskite when they are exposed to higher annealing temperatures. In a common procedure, perovskite phase originates from pyrochlore phase due to grain growth and nucleation mechanisms [76]. Therefore, the resulting pyrochlore peaks in 0.65PMN-0.35PT nanowires result from an incomplete crystallization of the sample. The resulting perovskite peaks for this lead-containing compound match precisely with those from standard card JPCDS of PMN-PT (no. 01-074-9392) and previous compounds reported in literature [60].

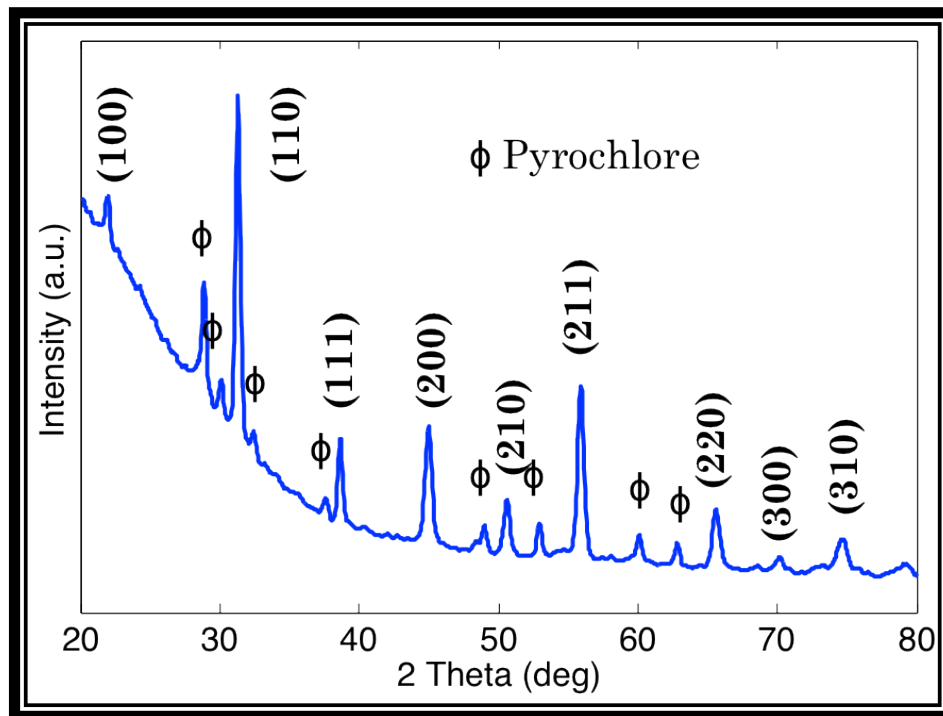


Figure 4.2. XRD patterns for as-spun 0.65PMN-0.35PT nanowires.

4.1.2 Morphology

The morphology of the synthesized NNO and 0.65PMN-0.35PT nanowires as well as BTO and PZT nanopowders are shown in Figure 4.3. It shown that NNO nanowires (Figure 4.3 (a)) have an average diameter of 400 nm and an average length of 20 μm . Because of these average dimensions, it may be assumed that the as-prepared NNO nanowires presented an aspect ratio of 50; therefore, these ceramic fillers are considered 1-D nanostructures. Every hydrothermal reaction displayed elevated densities of NNO nanowires. The resulting 0.65PMN-0.35PT nanofibers (Figure 4.3 (b)) displayed an average diameter of 100 nm after being dried at 200°C for a period of 2 hours. Due to the nature of the as-spun fibers, length calculations for 0.65PMN-0.35PT nanowires were neglected. Commercial ceramic fillers displayed powder morphology but varied diameters. Initially, commercial PZT powders (Figure 4.3 (c)) exhibited diameters between 500 nm and 1 μm . This values where reduced during the dispersion process. Commercial BTO nanopowders (Figure 4.3 (d)) displayed mean diameters below 50 nm, as specified by the supplier.

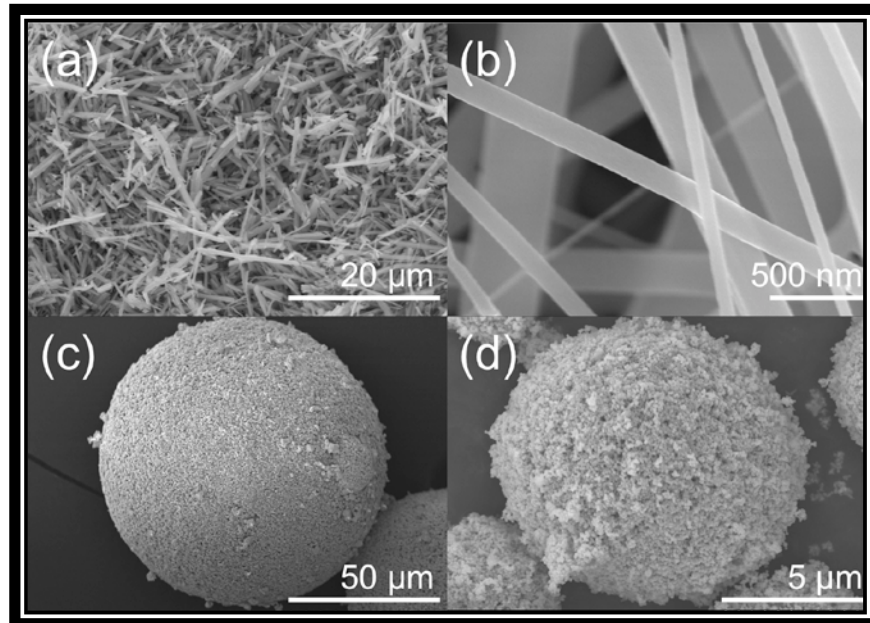


Figure 4.3. SEM images for the synthesized nanowires as well as commercial nanopowders: (a) NNO nanowires, (b) 0.65PMN-0.35PT nanowires, (c) PZT nanopowders, and (d) BTO nanopowders.

Dispersion of NNO nanowires in PVDF matrix is exhibited in Figure 4.4. As indicated by the SEM images, ceramic nanowires were homogeneously dispersed throughout the entire sample. The effect of volume fraction percentage increment is noticeable since the amount of nanofillers across the entire area of the polymer matrix was increased. As expected, NNO nanowires displayed a random orientation inside the PVDF matrix, similar to those previously reported in literature [77,78]. Because of the hot-press process, flat surfaces with constant thickness were achieved. Regardless of this heat treatment, nanocomposites with no void, cracks, vacancies, or any external damage were obtained. Besides SEM images, a digital view of NNO/PVDF and 0.65PMN-0.35PT/PVDF nanocomposites is shown in Figure 4.5.

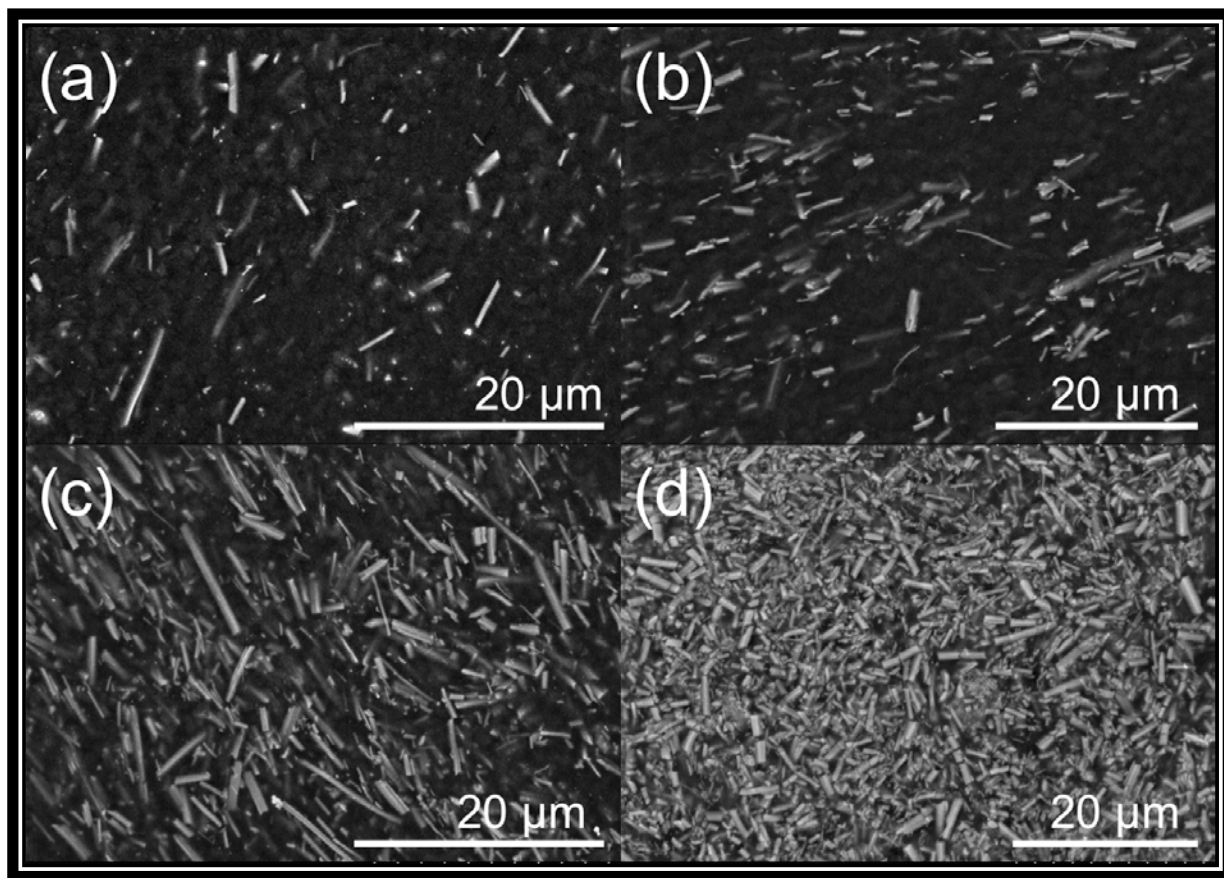


Figure 4.4. SEM images of NNO/PVDF nanocomposites with different volume fraction percentages: (a) NNO/PVDF 5%, (b) NNO/PVDF 10%, (c) NNO/PVDF 20%, and (d) NNO/PVDF 30%.

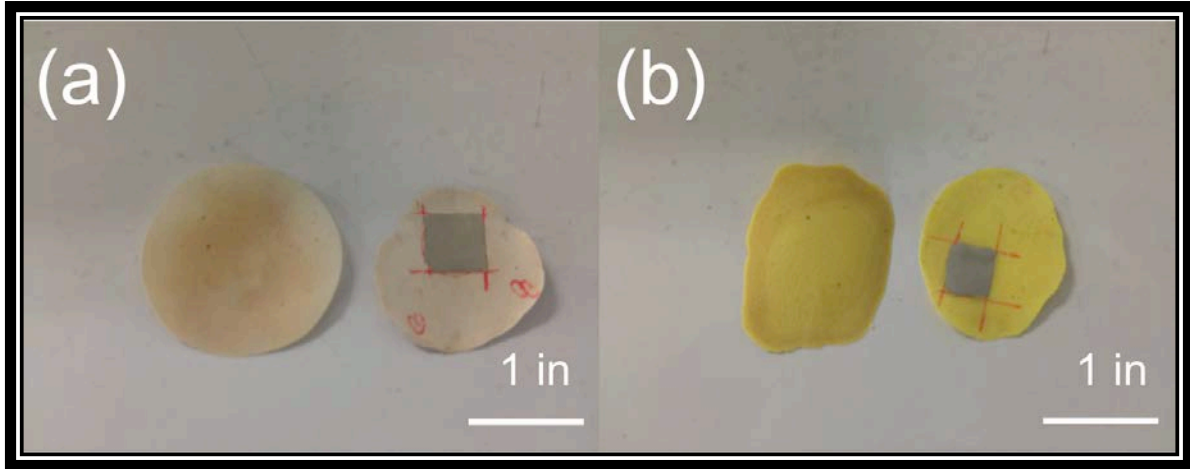


Figure 4.5. Digital view of the as-prepared nanocomposites with and without silver paint electrodes: (a) NNO/PVDF and (b) 0.65PMN-0.35PT/PVDF.

The dispersion of 0.65PMN-0.35PT nanofibers as well as commercial PZT and BTO nanopowders are shown in Figure 4.6. Similarly to NNO/PVDF nanocomposites, these composites displayed homogeneous dispersion of ceramic fillers as well as random orientations. Opposite to NNO nanowires, 0.65PMN-0.35PT nanofibers displayed powder morphologies inside the PVDF matrix. This may be due to the stress applied during the dispersion and solution casting process, resulting in fragmentation of initial nanofibers. Figures 4.6 (c) and 4.6 (d) display 30% BTO/PVDF and PZT/PVDF nanocomposites, respectively. Both samples displayed a good dispersion of ceramic fillers, but few agglomerations are visible especially in BTO/PVDF composite. These SEM images demonstrate the reduction in diameter of commercial powders after the solution casting process, being PZT nanopowders the ones displaying higher diameters again.

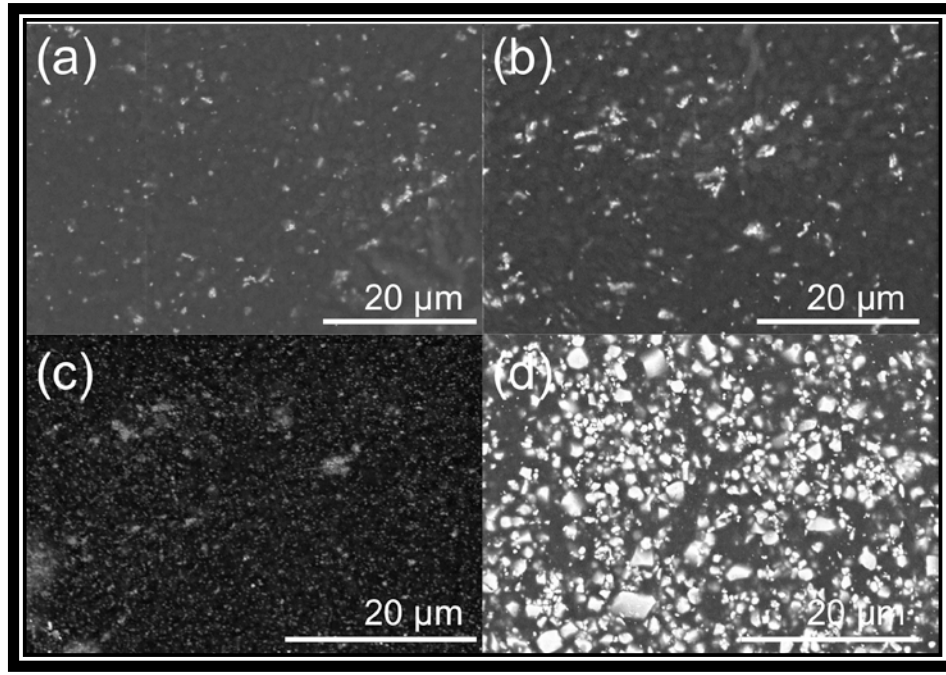


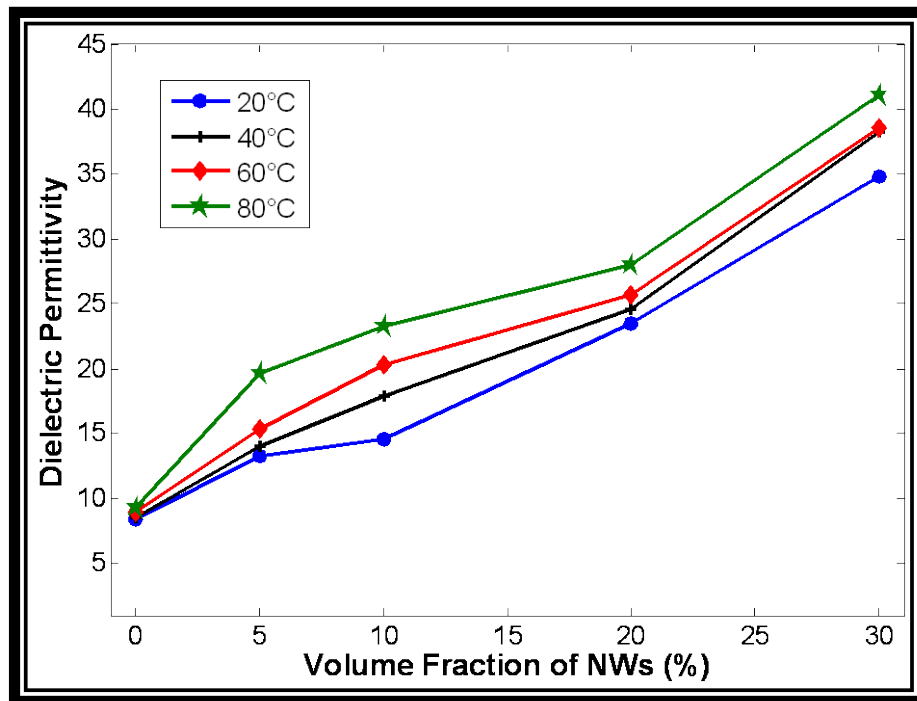
Figure 4.6. SEM images for nanocomposites containing 0.65PMN-0.35PT and commercial ceramics: (a) 5% 0.65PMN-0.35PT/PVDF, (b) 10% 0.65PMN-0.35PT/PVDF, (c) 30% BTO/PVDF, and (d) 30% PZT/PVDF.

4.2 ELECTRICAL PROPERTIES OF NANOCOMPOSITES

Followed by the fabrication of nanocomposites, the electrodes were applied on top and bottom surfaces of the samples to form capacitors in parallel plate fashion, where the energy density is defined by:

$$W = \frac{1}{2} \epsilon_0 \epsilon_r E_{od}^2$$

where



To characterize the influence of nanowire volume fraction on relative dielectric constant, dielectric constants of various volume fractions nanocomposites under a frequency of 1 kHz at temperatures of 20 and 60°C are tested and shown in Figure 4.8 and Figure 4.9, respectively. Results demonstrated an increment in the dielectric permittivity of the nanocomposites as the volume fraction increased; due to the high dielectric constants of ceramic fillers, which are about two orders of magnitude higher than that of PVDF matrix [81]. Among the tested nanocomposites, NNO nanocomposites have shown higher dielectric constant under all volume fractions. This is because the relative dielectric constant of bulk NNO (209) and the effect of 1-D nanowires [82]. The average dielectric value exhibited by 30% NNO/PVDF nanocomposites at 20°C is 34.82, 29.96% higher than that of the 30% PZT/PVDF nanocomposites, and 69.44% higher than that of BTO/PVDF nanocomposites. At 60°C, 30% NNO/PVDF presented a permittivity constant of 38.61, resulting in a 32.66% increment when compared to its closer competitor, 30% PZT/PVDF. Finally, the low dielectric values displayed by 0.65PMN-0.35PT/PVDF nanocomposites are due to its low crystallinity and presence of pyrochlore peaks.

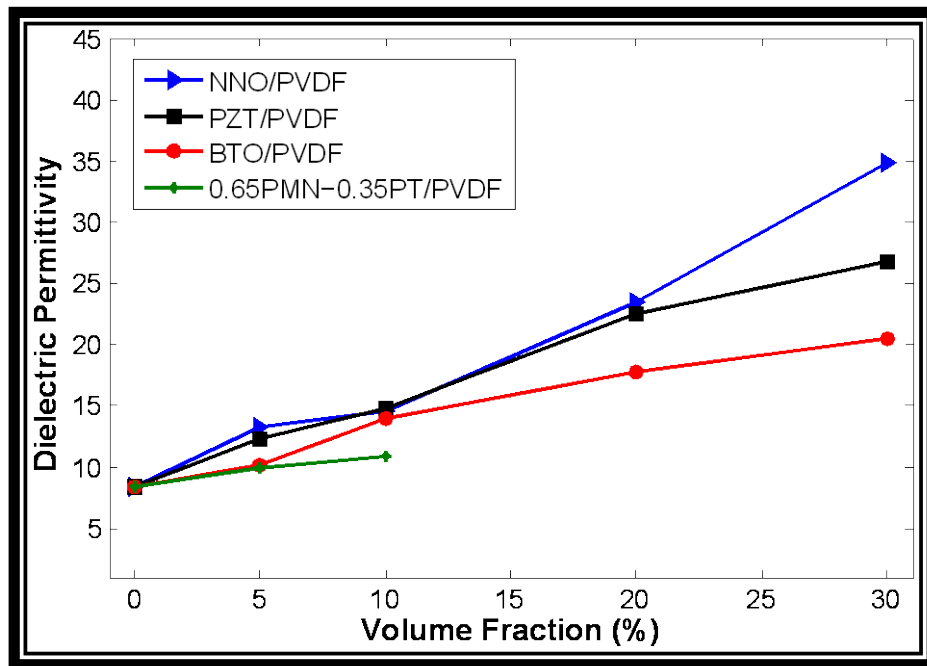


Figure 4.8. Dielectric permittivity constants of various nanocomposite capacitors at a temperature of 20°C and a frequency of 1 kHz.

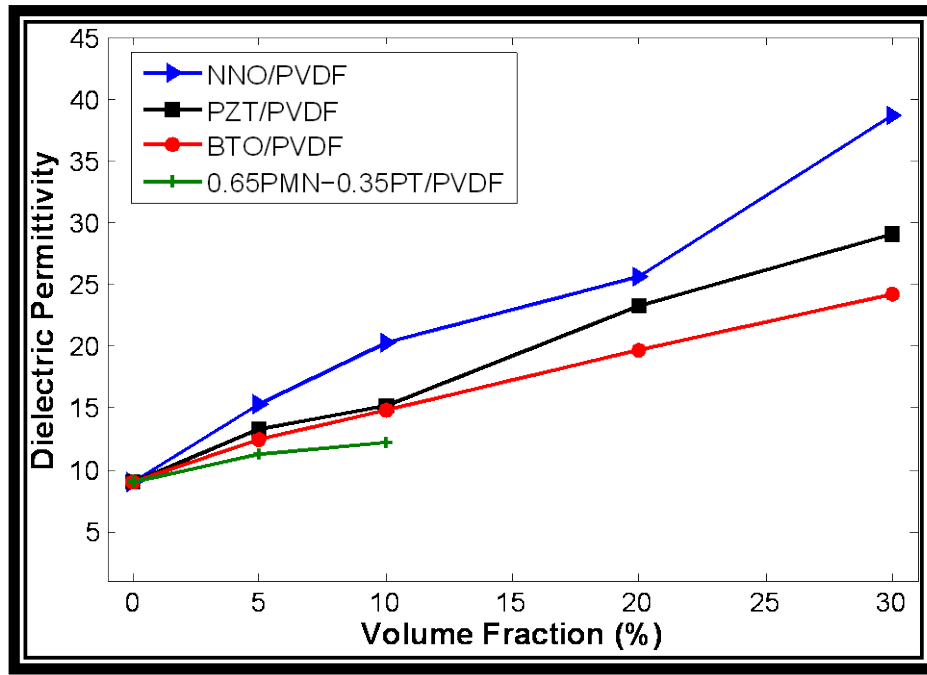


Figure 4.9. Dielectric permittivity constants of various nanocomposite capacitors at a temperature of 60°C and a frequency of 1 kHz.

One of the applications for dielectric capacitors is for high frequency charge and discharge, therefore, the influence of dielectric constant under high frequencies must be characterized. The relationship between dielectric permittivity constant and frequency is shown in Figures 4.10. All of the dielectric nanocomposites displayed similar behaviors under a frequency range between 1 kHz and 1 MHz and a temperature of 20°C. As frequency increases, dielectric permittivity of the nanocomposites decreases regardless its volume fraction. This same behavior has been previously documented in literature [83,84]. The general trend demonstrates an exponential decay of dielectric constant; this reduction is more abrupt between 1 kHz and 5 kHz. Nanocomposites with 20% and 30% volume fraction values displayed a faster reduction in dielectric permittivity when compared with 5% and 10% samples. When compared with BTO, PZT, and 0.65PMN-0.35PT samples, NNO nanocomposites displayed higher dielectric values among frequencies of 1-10 kHz. For frequencies above 10 kHz, PZT/PVDF samples exhibited a slight increment when compared to NNO/PVDF.

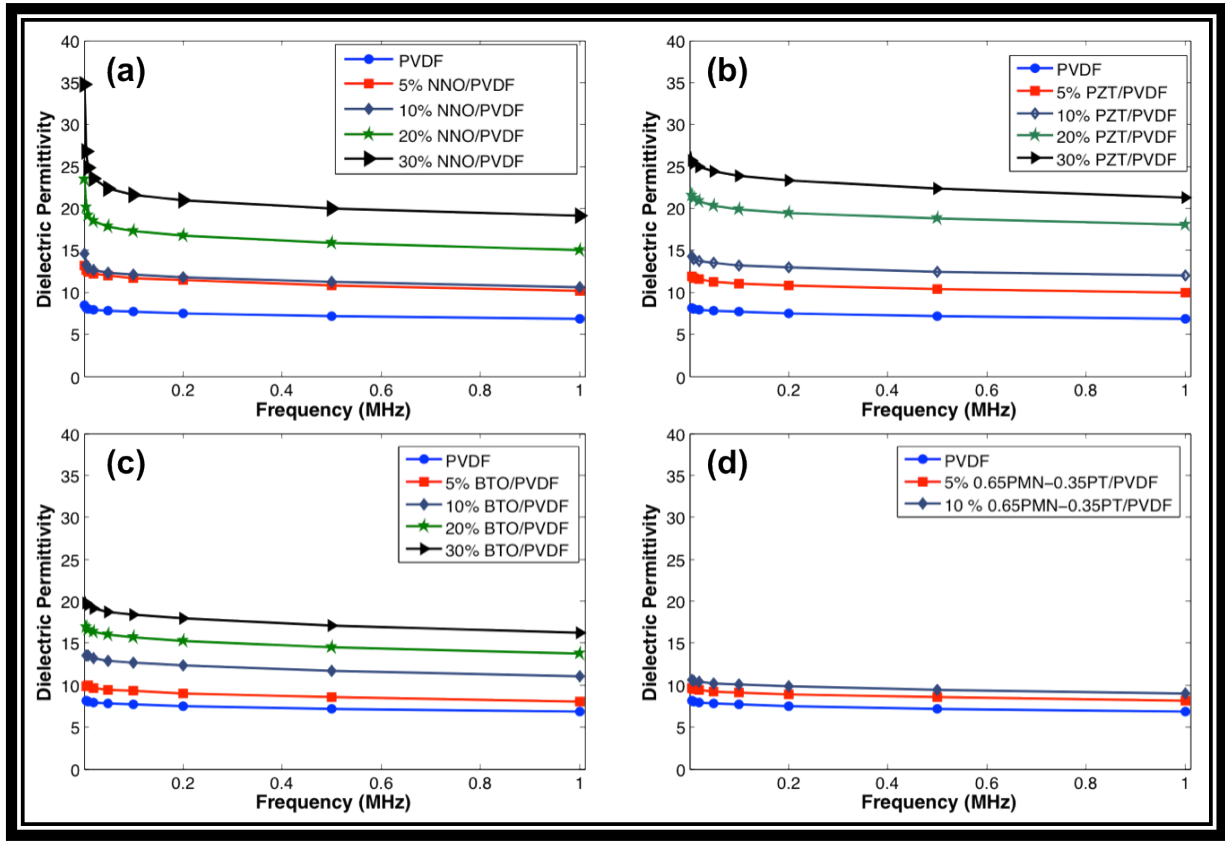


Figure 4.10. Dielectric permittivity constant of nanocomposites between a frequency range of 1 kHz-1 MHz at 20°C: (a) NNO/PVDF, (b) PZT/PVDF, (c) BTO/PVDF, and (d) 0.65PMN-0.35PT/PVDF.

Another important property of dielectric capacitors is the dielectric loss, which is a measurement of energy dissipation and degradation of material's insulation [85]. Therefore, the dielectric loss at a frequency of 1 MHz of the nanocomposites under different volume fractions is measured and shown in Figure 4.11. From the behavior of most of the samples, we can demonstrate that an increment in volume fraction of filler results in a decrease in energy dissipation, except for 30% PZT/PVDF nanocomposites, which display an increment up to 0.1224. This is mainly due to the lower dielectric loss of ceramic reinforcements, compared with polymer matrix. From Figure 4.11 it is shown that 30% NNO/PVDF nanocomposites displayed lower dielectric loss when compared to other nanocomposites with 30% volume fraction of fillers.

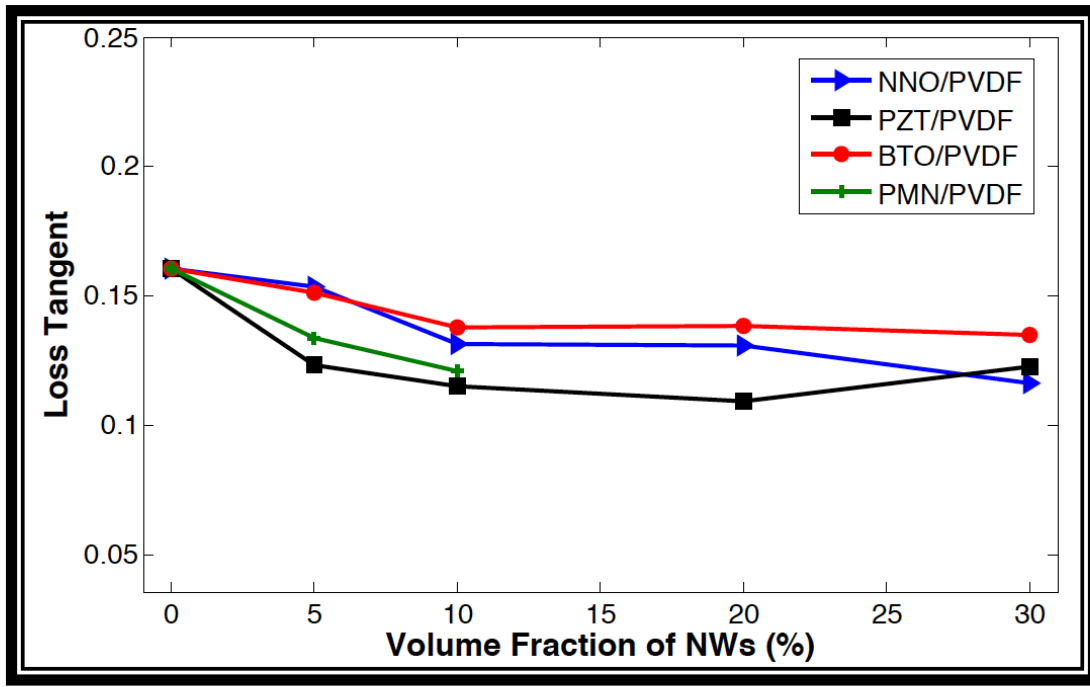


Figure 4.11. Dielectric loss at 1 MHz of nanocomposites as a function of filler volume fraction.

After the characterization of the dielectric permittivity and dielectric loss of the nanocomposites, breakdown strength testing was performed in order to fully understand the energy density of these dielectric film capacitors. Figure 4.12 shows the dielectric strength of the as-prepared NNO/PVDF nanocomposites at a temperature range within 20 and 80°C. Pure PVDF matrix displayed a breakdown voltage of 299 MV/m. Since the breakdown strength of PVDF is orders of magnitude higher than the nanowire inclusions, the dielectric strength decreases with the increment of volume fraction at all temperature ranges. 30% NNO/PVDF nanocomposites displayed a breakdown voltage of 63.463 MV/m. This reduction in dielectric strength is mainly due to the presence of low breakdown strength nanofillers inside the polymer matrix, as well as to a series of defects or imperfections within the nanocomposites as a result of the solution casting process [77]. Regardless of the high dielectric permittivity values displayed by NNO/PVDF nanocomposites at higher temperatures, the breakdown strength for these lead-free nanocomposites decreased when exposed to higher temperature ranges.

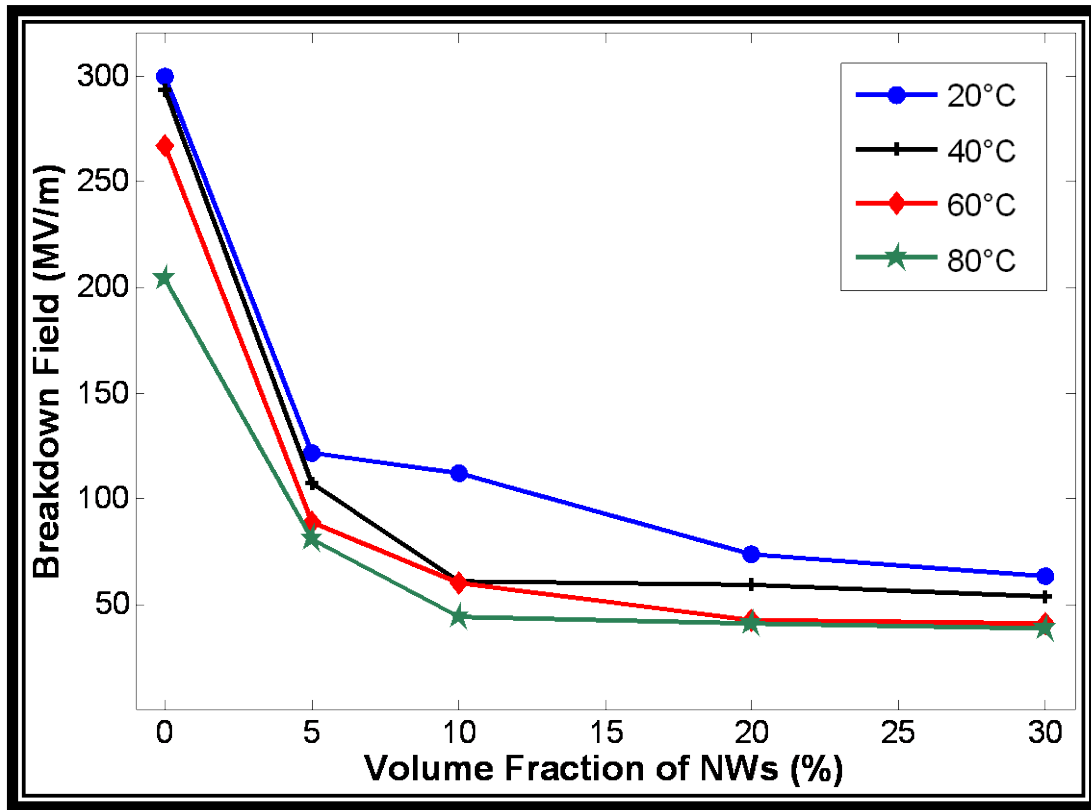


Figure 4.12. Breakdown strength of NNO/PVDF nanocomposites as a function of nanowires volume fraction percentage and temperature.

The breakdown strength results for NNO/PVDF nanocomposites were compared with those values for the control group as well as for 0.65PMN-0.35PT/PVDF nanocomposites. Figure 4.13 and 4.14 show the influence of volume fraction percentage over the breakdown strength at temperatures of 20 and 60°C, respectively. Similar to previous research, the dielectric strength values are reduced due to an increment in temperature and ceramic fillers [80,86]. Additionally, the increase of nanofillers is responsible for the agglomeration of particles, resulting in the formation of clusters responsible for facilitating a series of short-circuits affecting the breakdown strength [83]. Lead-containing nanocomposites displayed higher values when compared to lead-free samples. Initially, 5% PZT/PVDF composites displayed an increment of 27.73% and 17.11% when compared with NNO/PVDF at 20 and 60°C, respectively. At a volume fraction of 30%, PZT/PVDF exhibited increments of 37.75% and 73.13% over NNO/PVDF nanocomposites at 20 and 60°C, respectively. Therefore, a wider gap in the

dielectric strength between lead-containing and lead-free samples is visible at higher volume fraction percentages.

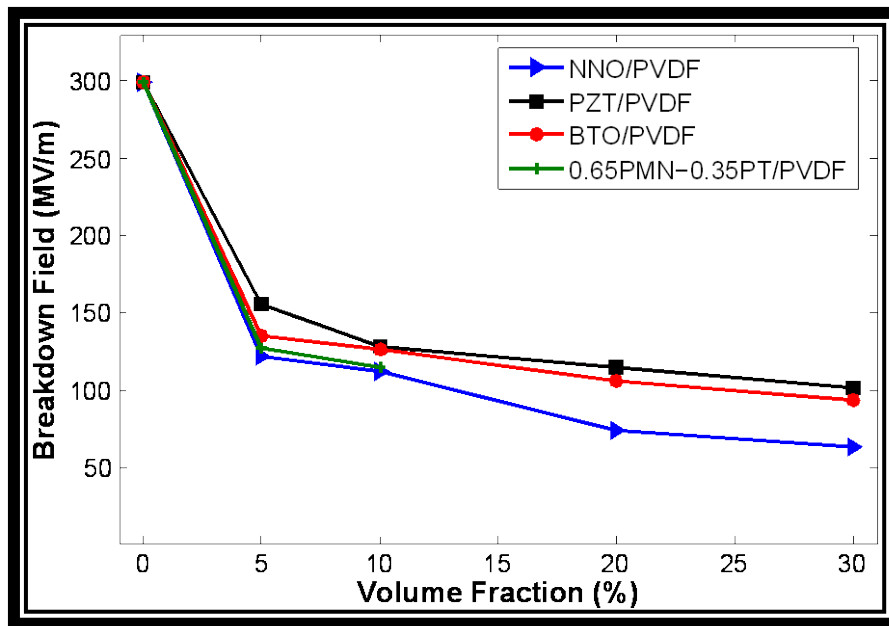


Figure 4.13. Breakdown strength values of various nanocomposites at 20°C.

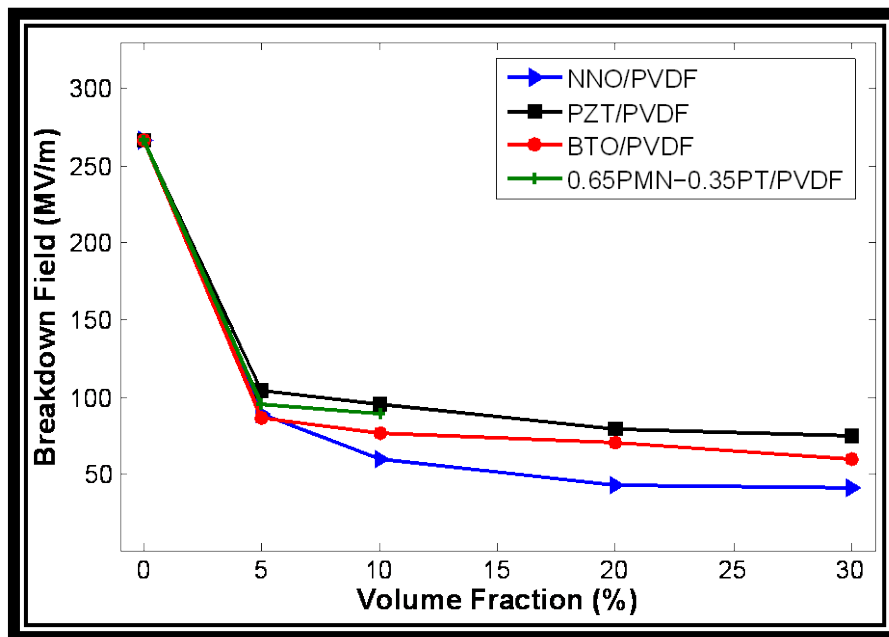


Figure 4.14. Breakdown strength values of various nanocomposites at 60°C.

The maximum energy densities for NNO/PVDF nanocomposites are shown in Figure 4.15. These energy values were computed from the experimental results obtained for the dielectric constants

recorded at a frequency of 1 kHz and the breakdown strengths. As stated in previous literature, breakdown strength plays a more important role than dielectric permittivity (square versus linear) while computing energy density of a capacitor [87]. Although the dielectric permittivity of NNO/PVDF nanocomposites increased with the temperature increment, the breakdown voltage exhibited a significant reduction, resulting in lower energy density values. Initially, all the nanocomposites displayed an abrupt reduction in breakdown strength values due to the presence of low dielectric strength ceramic nanofillers in a polymer matrix. At low volume fractions the effect of breakdown strength dominates the resulting energy density values, while at elevated volume fractions higher dielectric constants are responsible for the slight increment in energy density. Compared with previously developed 1-D PZT/PVDF nanocomposites, the NNO/PVDF displayed similar energy densities. Between the volume fraction range of 20% and 30%, the minimum and maximum differences in terms of energy density between PZT/PVDF and NNO/PVDF randomly oriented nanocomposites are 5.82 and 12.9%, respectively [88].

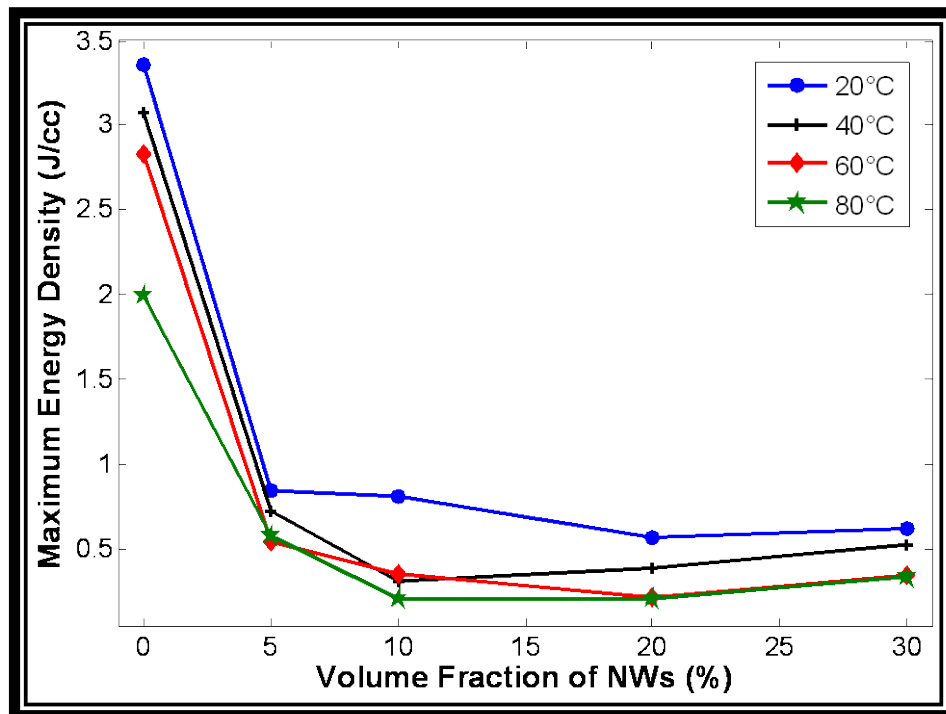


Figure 4.15. Maximum energy density for NNO/PVDF nanocomposites as a function of volume fraction percentage.

The energy density results for all other nanocomposites are shown in Figure 4.16 and 4.17. Among all of the polymer nanocomposite capacitors, PZT/PVDF samples displayed higher energy density values. Regardless of the temperature range, all of the nanocomposites initially displayed a sudden reduction in energy density once nanofillers were introduced into the polymer matrix. At volume fraction percentages of 20 and 30%, it is visible a trend suggesting an increment in energy density when compared to those nanocomposites containing 5% of ceramic fillers. 30% NNO/PVDF nanocomposites displayed energy densities of 0.6206 and 0.2919 J/cm³ at temperatures of 20 and 60°C, respectively. Compared to 30% PZT/PVDF nanocomposites, which presented the highest energy density results for these dielectric capacitors, 30% NNO/PVDF displayed a reduction in energy density of 49.54 and 58.97%. The maximum energy density obtained from these nanocomposites was of 1.2302 J/cm³ and belonged to 30% PZT/PVDF nanocomposites. The resulting energy density values for these lead-free advanced capacitors are still below previously developed nanocomposites, therefore, further modifications are required for improving the efficiency of these energy storage systems [19,77,89,90].

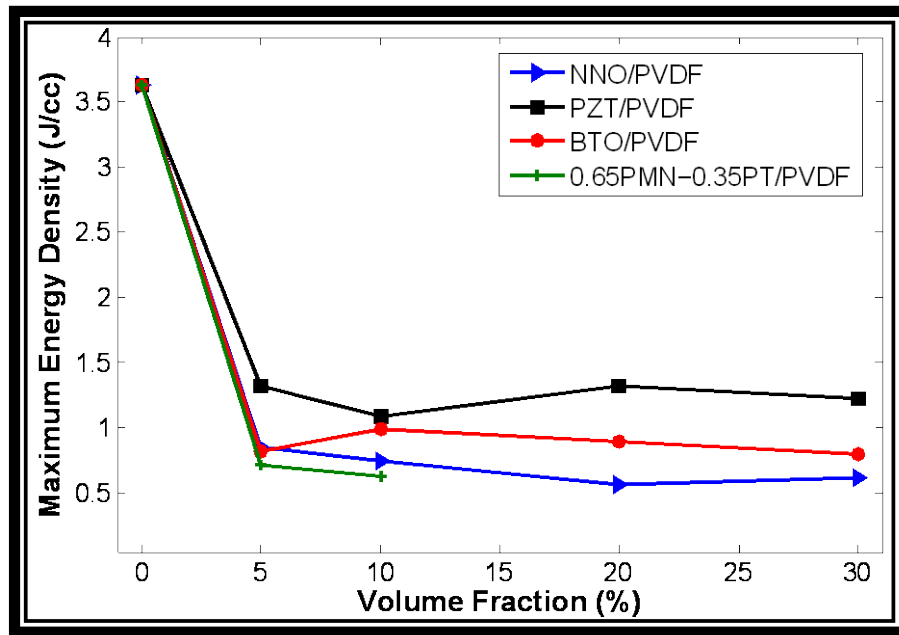


Figure 4.16. Maximum energy density of advanced dielectric capacitors as a function of volume fraction percentage at 20°C.

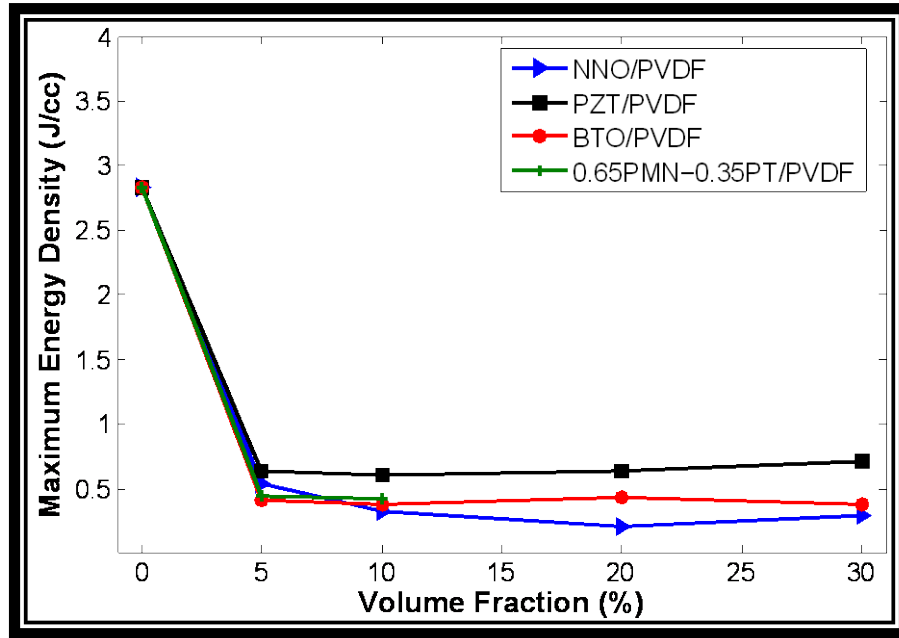


Figure 4.17. Maximum energy density of advanced dielectric capacitors as a function of volume fraction percentage at 60°C.

Since weight is equally important as volume in modern material system design, the mass energy or specific density for NNO/PVDF nanocomposites is exhibited in Figure 4.18. This calculated value is intended to demonstrate the amount of energy stored as a function of mass. As expected from the maximum energy calculations, the specific energy displayed a reduction with the increment of ceramic fillers. Similar to the energy density results, specific energy values displayed a slight increment at a volume fraction of 30% when compared to 10 and 20%. The maximum mass energy density recorded for NNO/PVDF nanocomposites corresponds to 30% samples and was 0.2419 J/g. Compared to the control group, NNO/PVDF displayed lower values when compared to PZT and BTO composites. Similarly to breakdown strength and energy density, the specific energy for these samples was reduced when exposed to elevated temperatures. At a temperature of 20°C, 30% PZT/PVDF nanocomposites displayed an increment of 44.52% when compared to 30% NNO/PVDF. This difference was incremented by a 77.58% at a temperature of 60°C.

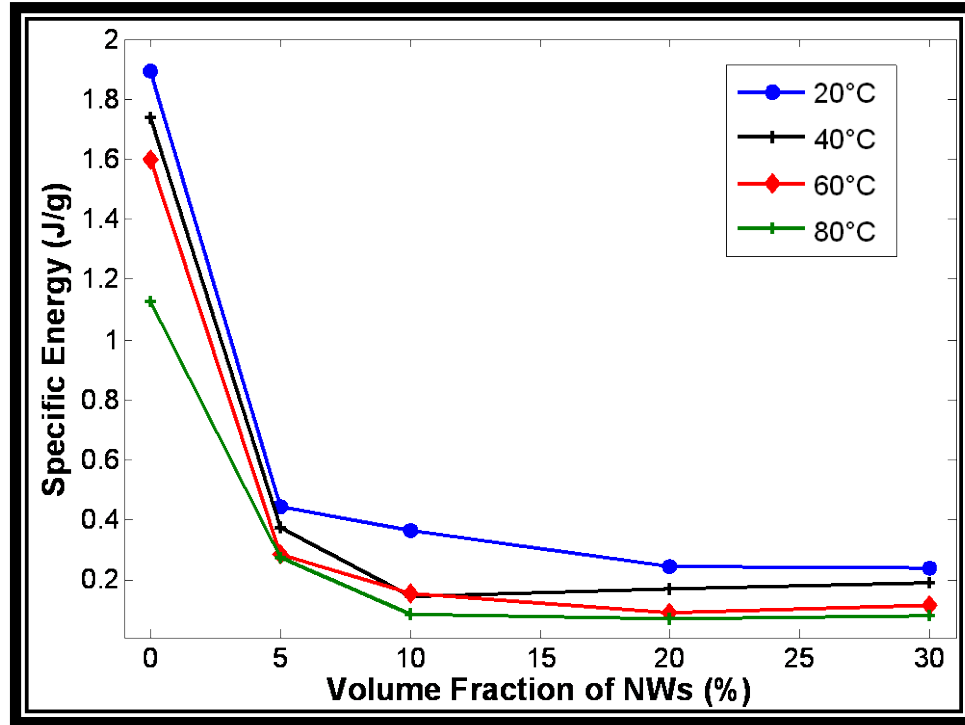


Figure 4.18: Specific energy for NNO/PVDF nanocomposites as a function of volume fraction.

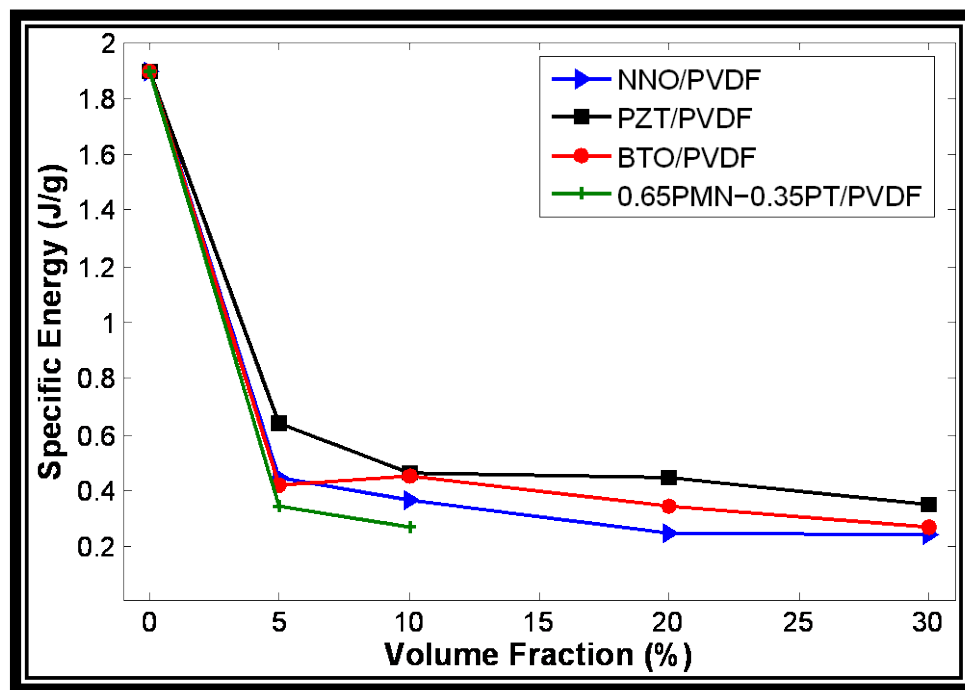


Figure 4.19: Specific energy for nanocomposites as a function of volume fraction at 20°C.

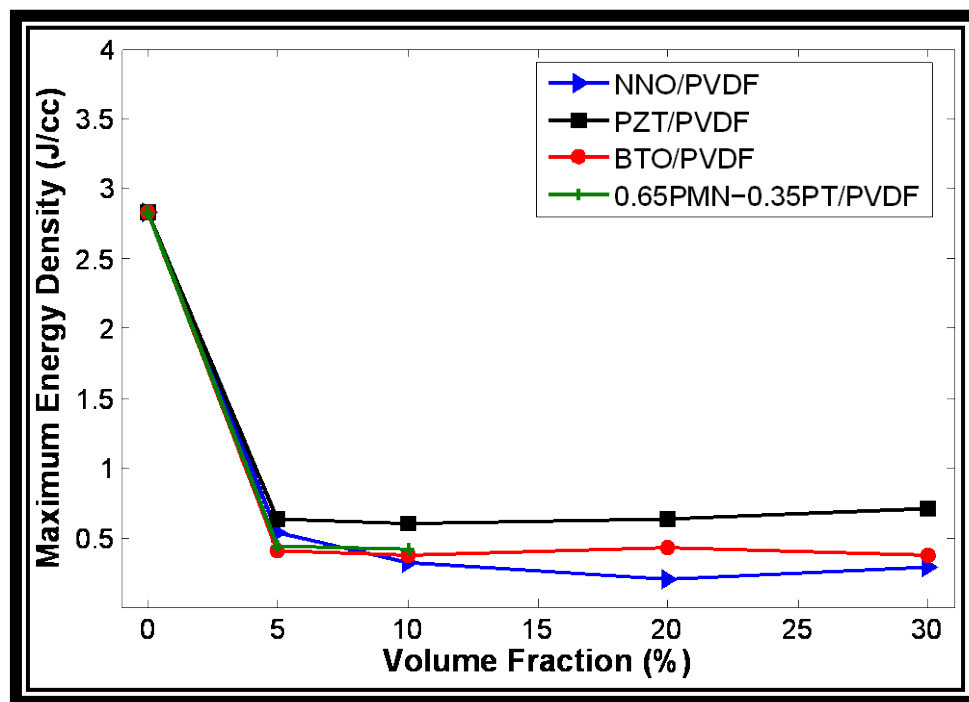


Figure 4.20: Specific energy for nanocomposites as a function of volume fraction at 60°C.

Chapter 5: Conclusion

This research effort introduced the fabrication and characterization of nanocomposite dielectric capacitors based on NaNbO_3 and $(1-x)\text{Pb}(\text{Mg}_{1/3}\text{Nb}_{2/3})\text{O}_3$ - $x\text{PbTiO}_3$ nanowires embedded in PVDF matrix. This nanocomposite approach has demonstrated the feasibility of enhancing the physical and electrical properties of both, ceramic fillers and polymer film matrices. The resulting $\text{NaNbO}_3/\text{PVDF}$ nanocomposites have displayed higher dielectric permittivity values than $(1-x)\text{Pb}(\text{Mg}_{1/3}\text{Nb}_{2/3})\text{O}_3$ - $x\text{PbTiO}_3/\text{PVDF}$, $\text{Pb}(\text{Zr}_{1-x}\text{Ti}_x)\text{O}_3/\text{PVDF}$ and $\text{BaTiO}_3/\text{PVDF}$. Also, the dielectric loss of $\text{NaNbO}_3/\text{PVDF}$ composites is lower than that of those containing commercial nanopowders or $(1-x)\text{Pb}(\text{Mg}_{1/3}\text{Nb}_{2/3})\text{O}_3$ - $x\text{PbTiO}_3$ nanowires. $\text{NaNbO}_3/\text{PVDF}$ nanocomposites have exhibited energy density values up to 0.8511 J/cm^3 , resulting in higher energy density capability when compared to current polymer film and ceramic dielectric capacitors ($<0.60 \text{ J/cm}^3$). Current results have demonstrated the feasibility of employing this type of energy storage devices under working conditions with temperatures above room temperature. Further surface functionalization and inclusion alignment methods as previously reported could significantly enhance the energy density of the lead-free nanocomposite capacitors. Therefore, this research effort has shown the feasibility of expelling lead from high dielectric constant and high energy density capacitors.

References

- [1] Bruce, P. G., Scrosati, B., and Tarascon, J. M. "Nanomaterials for rechargeable lithium batteries". *Angewandte Chemie International Edition*, vol. 47, no. 16, pp. 2930-2946, 2008.
- [2] Winter, M. and Brodd, R. J. "What are batteries, fuel cells, and supercapacitors". *Chemical Reviews*, vol. 104, no. 10, pp. 4245-4269, 2004.
- [3] Conway, B. E. *Electrochemical supercapacitors: scientific fundamentals and technological application*. New York: Kluwer Academic / Plenum Publishers, 1999.
- [4] Ginley, D. S., and Cahen, D. *Fundamentals of materials for energy and environmental sustainability*. New York : Materials Research Society , 2012.
- [5] Wang, Q., Wen, Z., and Li, J. "A hybrid supercapacitor fabricated with a carbon nanotube cathode and TiO₂-B nanowire anode". *Advanced Functional Materials*, vol. 16, no. 16, pp. 2141-2146, 2006.
- [6] Halper, M. S., and Ellenbogen, J. C. "Supercapacitors: a brief overview". Report No. MP05W0000272, The MITRE Corporation, McLean, Virginia, 2006.
- [7] Dummer, G. W. A. *Electronic inventions and discoveries: electronics from its earliest beginnings to the present day*. 4th Edition. Bristol, UK: Institute of Physics Publishing, 1997.
- [8] Ho, J., Jow, T. R., and Boggs, S. "Historical introduction to capacitor technology". *IEEE Transactions on Electrical Insulation Magazine*, vol. 26, no. 1, pp. 20-25, 2010.
- [9] Cohen, I. B. *Dictionary of scientific biography*. vol. 5, Gillispie, C. C., Ed. New York: Charles Scribner's Sons, 1972.
- [10] Longland, T., Hunt, T. W., and Brecknell, W. A. *Power capacitor handbook*. London, UK: Butterworth, 1984.
- [11] Jayalakshmi, M. and Balasubramanian, K. "Simple capacitors to supercapacitor – an overview". *International Journal of Electrochemical Science*, vol. 3, no. 11, pp. 1196-1217, 2008.
- [12] Nishino, A. "Capacitors: operating principles, current market and technical trends". *Journal of Power Sources*, vol. 60, no. 2, pp. 137-147, 1996.
- [13] Wang, G., Zhang, L., and Zhang, J. "A review of electrode materials for electrochemical supercapacitors". *Chemical Society Reviews*, vol. 41, no. 2, pp. 797-828, 2012.
- [14] Aricò, A. S., Bruce, P., Scrosati, B., Tarascon, J. M., and van Schalkwijk, W. "Nanostructured materials for advanced energy conversion and storage devices". *Nature Materials*, vol. 4, no. 5, pp. 366-377, 2005.
- [15] Conway, B. E., Birrs, V., and Wojtowicz, J. "The role of utilization of pseudocapacitors for energy storage by supercapacitors". *Journal of Power Sources*, vol. 66, no. 1-2, pp. 1-14, 1997.
- [16] Chen, H., Cong, T. N., Yang, W., Tan, C., Li, Y., and Ding, Y. "Progress in electrical energy storage system: a critical review". *Progress in Natural Science*, vol. 19, no. 3, pp. 291-312, 2009.
- [17] Burke, A. "Ultracapacitors: why, how, and where is the technology". *Journal of Power Sources*, vol. 91, no. 1, pp. 37-50, 2000.
- [18] Winsor IV, P., Lobo, E., Munshi, M. Z., and Ibrahim, A. "New polymer dielectric for high energy density film capacitors".
- [19] Wang, Y., Zhou, X., Chen, Q., Chu, B., and Zhang, Q. "Recent development of high energy density polymers for dielectric capacitors". *IEEE Transactions on Dielectrics and Electrical Insulation*, vol. 17, no. 4, pp. 1036-1042, 2010.
- [20] Lehmann, P. "Overview of the electric launch activities at the French-German research institute of Saint-Louis (ISL)". *IEEE Transactions on Magnetics*, vol. 39, no. 1, pp. 24–28, 2003.
- [21] Drobny, J. G. *Polymers for electricity and electronics: materials, properties, and applications*. New Jersey: John Wiley & Sons, Inc., 2012.

- [22] Rödel, J., Jo, W., Seifert, K. T. P., Anton, E. M., and Granzow, T. "Perspective on the development of lead-free piezoceramics". *Journal of the American Ceramic Society*, vol. 92, no. 6, pp. 1153-1177, 2009.
- [23] Shrout, T. R. and Zhang, S. J. "Lead-free piezoelectric ceramics: alternatives for PZT". *Journal of Electroceramics*, vol. 19, no. 1, pp. 113-126, 2007.
- [24] Guillon, O., Chang, J., Schaab, S., and Kang, S. J. L., "Capacitance enhancement of doped barium titanate dielectrics and multilayer ceramic capacitors by a post-sintering thermo-mechanical treatment," *Journal of the American Ceramic Society*, vol. 95, no. 7, pp. 2277–2281, 2012.
- [25] Nalwa, H. *Handbook of Low and High Dielectric Constant Materials and Their Applications*. London, UK: Academic Press, 1999.
- [26] Cai, H., Gui, Z., and Li, L. "Low-sintering composite multilayer ceramic capacitors with X7R specification". *Materials Science and Engineering: B*, vol. 83, no. 1-3, pp. 137-141, 2001.
- [27] Nelson, J. K., ed. *Dielectric Polymer Nanocomposites*. New York: Springer, 2010.
- [28] Zhou, W., Liu, H., Boughton, R. I., Du, G., Lin, J., Wang, J., and Liu, D. "One-dimensional single-crystalline Ti-O based nanostructures: properties, synthesis, modifications and applications". *Journal of Materials Chemistry*, vol. 20, no. 29, pp. 5993-6008, 2010.
- [29] Meyyappan, M. and Sunkara, M. K. *Inorganic nanowires: applications, properties, and characterization*. Boca Raton, FL: CRC Press, 2010.
- [30] Ashby, M. F., Ferreira, P., and Schodek, D. L. *Nanomaterials, nanotechnologies and design: an introduction for engineers and architects*. Burlington, MA: Butterworth-Heinemann, 2009.
- [31] Cao, G. and Wang, Y. "Nanostructures and Nanomaterials: Synthesis, Properties, and Applications". 2nd Edition. World Scientific, Singapore, 2011.
- [32] Tiwari, J. N., Tiwari, R. N., and Kim, K. S. "Zero-dimensional, one-dimensional, two-dimensional, and three-dimensional nanostructured materials for advanced electrochemical energy devices". *Progress in Materials Science*, vol. 57, no. 4, pp. 724-803, 2012.
- [33] Bhalla, A. S., Guo, R., and Roy, R. "The perovskite structure-a review of its role in ceramic science and technology". *Materials Research Innovations*, vol. 4, no. 1., pp. 3-26, 2010.
- [34] Barsoum, M. W. *Fundamentals of ceramics*. New York: Taylor & Francis, 2003.
- [35]

- [42] Byrappa, K. and Yoshimura, M. *Handbook of hydrothermal technology: A technology for crystal growth and materials processing*. New Jersey: Noyes Publications, 2001.
- [43] Feng, S. and Xu, R. “New materials in hydrothermal synthesis”. *Accounts of Chemical Research*, vol. 34, no. 3, pp. 239-247, 2001.
- [44] Knauth, P. and Schoonman, J., Ed. *Nanostructured materials: selected synthesis methods, properties, and applications*. New York: Kluwer Academic Publishers, 2004.
- [45] Chen, X. and Mao, S. S. “Synthesis of titanium dioxide (TiO₂) nanomaterials”. *Journal of Nanoscience and Nanotechnology*, vol. 6, no. 4, pp. 906-925, 2006.
- [46] Schubert, U. and Hüsing, N. *Synthesis of inorganic materials*. 3rd Ed. Weinheim, Germany: Wiley-VCH, 2012.
- [47] Yoshimura, M. and Byrappa, K. “Hydrothermal Processing of materials: past, present, and future”. *Journal of Materials Science*, vol. 43, no. 7, pp. 2085-2103, 2008.
- [48] Wang, Y., Wu, M., and Zhang, W. F. “Preparation and electrochemical characterization of TiO₂ nanowires as an electrode material for lithium-ion batteries”. *Electrochimica Acta*, vol. 53, no. 27, pp. 7863-7868, 2008.
- [49] Wu, F., Wang, Z., Li, X., and Guo, H. “Hydrogen titanate and TiO₂ nanowires as anode materials for lithium-ion batteries”. *Journal of Materials Chemistry*, vol. 21, no. 34, pp. 12675-12681, 2011.
- [50] Myung, S. T., Takahashi, N., Komaba, S., Yoon, C. S., Sun, Y. K., Amine, K., and Yashiro, H. “Nanostructured TiO₂ and its applications in lithium-ion storage”. *Advanced Functional Materials*, vol. 21, no. 17, pp. 3231-3241, 2011.
- [51] Joshi, U. A. and Lee, J. S. “Template-free hydrothermal synthesis of single-crystalline barium titanate and strontium titanate nanowires”. *Small*, vol. 1, no. 12, pp. 1172-1176, 2005.
- [52] Grange, R., Choi, J. W., Hsieh, C. L., Pu, Y., Magrez, A., Smajda, R., Forro, L., and Psaltis, D. “Lithium niobate nanowires synthesis, optical properties, and manipulation”. *Applied Physics Letters*, vol. 95, no. 14, pp. 143105-3, 2009.
- [53] Magrez, A., Vasco, E., Seo, J. W., Dieker, C., Setter, N., and Forro, L. “Growth of single-crystalline KNbO₃ nanostructures”. *The Journal of Physical Chemistry B*, vol. 110, no. 1, pp. 58-61, 2006.
- [54] Shi, H., Li, X., Wang, D., Yuan, Y., Zou, Z., and Ye, J. “NaNbO₃ nanostructures: facile synthesis, characterization, and their photocatalytic properties”. *Catalysis Letters*, vol. 132, no. 1-2, pp. 205-212, 2009.
- [55] Xu, S., Poirier, G. and Yao, N. “PMN-PT nanowires with very high piezoelectric constant”. *Nano Letters*, vol. 12, no. 5, pp. 2238-2242, 2012.
- [56] Pierre, A. C. *Introduction to sol-gel processing*. 2nd Ed. Massachusetts: Kluwer Academic Publishers, 2002.
- [57] Bansal, N. P. and Boccaccini, A. R., Ed. *Ceramics and composites processing methods*. New Jersey: John Wiley & Sons, 2012.
- [58] Hench, L. L. and West, J. K. “The sol-gel process”. *Chemical Reviews*, vol. 90, no.1, pp. 72-93, 1990.
- [59] Brinker, C. J. and Scherer, G. W. *Sol-gel science: the physics and chemistry of sol-gel processing*. San Diego: Academic Press, 1990.
- [60] Calzada, M. L., Alguero, M., Ricote, J., Santos, A., and Pardo, L. “Preliminary results on sol-gel processing of <100> oriented Pb(Mg₁/3Nb₂/3)O₃-PbTiO₃ thin films using diol-based solutions”. *Journal of Sol-Gel Science and Technology*, vol. 42, no. 3, pp. 331-336, 2007.

- [61] Calzada, M. L., Alguero, M., Santos, A., Stewart, M., Cain, M. G., and Pardo, L. "Piezoelectric, ferroelectric $\text{Pb}(\text{Mg}_{1/3}\text{Nb}_{2/3})\text{O}_3\text{-PbTiO}_3$ thin films with compositions around the morphotropic phase boundary prepared by a sol-gel process of reduced thermal budget". *Journal of Materials Research*, vol. 24, no. 2, pp. 526-533, 2009.
- [62] Singh, S. and Krupanidhi, S. B., "Perovskite phase transformation in $0.65\text{Pb}(\text{Mg}_{1/3}\text{Nb}_{2/3})\text{O}_3\text{-}0.35\text{PbTiO}_3$ nanoparticles derived by sol-gel". *Journal of Applied Physics*, vol. 111, no. 2, pp. 024314, 2012.
- [63] Xu, X., Poirier, G., and Yao, N. "Fabrication and piezoelectric property of PMN-PT nanofibers". *Nano Energy*, vol. 1, no. 4, pp. 602-607, 2012.
- [64] Leng, J. and Lau, A., ed. "Multifunctional Polymer Nanocomposites", Boca Raton, FL: CRC Press, 2011.
- [65] Ibrahim, S., Al Jaafari, A. A., and Ayesh, A. S. "Physical characterizations of three phase polycarbonate nanocomposites". *Journal of Plastic Film and Sheeting*, vol. 27, no. 4, pp. 275-291, 2011.
- [66] Xie, L., Huang, X., Wu, C., and Jiang, P. "Core-Shell structured poly(methyl methacrylate)/ BaTiO_3 nanocomposites prepared by in situ atom transfer radical polymerization: a route to high dielectric constant materials with the inherent low loss of the base polymer". *Journal of Materials Chemistry*, vol. 21, no. 16, pp. 5897-5906, 2011.
- [67] Kim, P., Doss, N. M., Tillotson, J. P., Hotchkiss, P. J., Pan, M., Marder, S. R., Li, J., Calame, J. P., and Perry, J. W. "High energy density nanocomposites based on surface-modified BaTiO_3 and a ferroelectric polymer". *ACS Nano*, vol. 3, no.9, pp. 2581-2592, 2009.
- [68] Mao, Y. P., Mao, S. Y., Ye, Z., Xie, Z. X., and Zheng, L. S. "Size-dependences of the dielectric and ferroelectric properties of fluoride nanocomposites". *Journal of Applied Physics*, vol. 108, no. 1, pp. 014102-6, 2010.
- [69] Dang, Z.-M., Yuan, J.-K., Zha, J.-W., Zhou, T., Li, S.-T., Hu, G.-H. "Fundamentals, processes and applications of high-permittivity polymer-matrix composites". *Progress in Materials Science*, vol. 57, no. 4, pp. 660-723, 2012.
- [70] Ni, L. and Chen, X. M. "Dielectric relaxations and formation mechanism of giant dielectric constant step in $\text{CaCu}_3\text{Ti}_4\text{O}_{12}$ ceramics". *Applied Physics Letters*, vol. 91, no. 12, pp. 122905, 2007.
- [71] Chen, A., Kamata, K., Nakagawa, M., Iyoda, T., Wang, H., and Li, X. "Formation process of silver-polypyrrole coaxial nanocables synthesized by redox reaction between AgNO_3 and pyrrole in the presence of poly(vinylpyrrolidone)". *The Journal of Physical Chemistry B*, vol. 109, no. 39, pp. 18283-18288, 2005.
- [72] Das-Gupta, D. K. and Doughty, K. "Polymer-ceramic composite materials with high dielectric constants". *Thin Solid Films*, vol. 158, no. 1, pp. 93-105, 1988.
- [73] Jung, H. J., Lee, M., Hong, J. I., Ding, Y., Chen, C. Y., Chou, L. J., and Wang, Z. L. "Lead-free NaNbO_3 nanowires for high output piezoelectric nanogenerator". *ACS Nano*, vol. 5, no. 12, pp. 10041-10046, 2011.
- [74] ASTM Standard D149-09, "Standard test method for dielectric breakdown voltage and dielectric strength of solid electrical insulating materials at commercial power frequencies". Research Report, ASTM International, West Conshohocken, Pa, USA, 2009.
- [75] Ke, T. Y., Chen, H. A., Sheu, H. S., Yeh, J. W., Lin, H. N., Lee, C. Y., and Chiu, H. T., "Sodium niobate nanowire and its piezoelectricity". *Journal of Physical Chemistry C*, vol. 112, no. 24, pp. 8827-8831, 2008.

- [76] Singh, S. and Krupanidhi, S. B., "Perovskite phase transformation in 0.65Pb(Mg_{1/3}Nb_{2/3})O₃-0.35PbTiO₃ nanoparticles derived by sol-gel". *Journal of Applied Physics*, vol 111. no. 2, pp. 024314, 2012.
- [77] Tang, H., Lin, Y., Andrews, C., and Sodano, H. A., "Nanocomposites with increased energy density through high aspect ratio PZT nanowires". *Nanotechnology*, vol. 22, no. 1, Article ID 10041, 2011.
- [78] Vaughan, A. S., Swingler, S. G., and Zhang, Y., "Polyethylene nanodielectrics: the influence of nanoclays on structure formation and dielectric breakdown". *IEEE Transactions on Fundamental and Materials*, vol. 126, no. 11, pp. 1057-1063 (2006).
- [79] Li, J., Claude, J., Norena-Franco, L. E., Seok, S. I., and Wang, Q. "Electrical energy storage in ferroelectric polymer nanocomposites containing surface-functionalized BaTiO₃ nanoparticles". *Chemistry of Materials*, vol. 20, no. 20, pp. 6304-606, 2008.
- [80] Leng, J. and Lau, A., ed. "Multifunctional Polymer Nanocomposites", Boca Raton, FL: CRC Press, 2011.
- [81] Varadan, V. V., Roh, Y. R., Varadan, V. K., and Tancrrell, R. H., "Measurement of all the elastic and dielectric constants of poled PVDF films." *Proceedings of the IEEE Ultrasonics Symposium*, vol. 2, pp. 727-730, 1989.
- [82] Shanker, V. Samal, S. L., Pradhan, G. K., Narayana, C., and Ganguli, A. K., "Nanocrystalline NaNbO₃ and NaTaO₃: rietveld studies, Raman spectroscopy and dielectric properties". *Solid State Sciences*, vol. 11, no. 2, pp. 562-569, 2009.
- [83] Gallone, G. Carpi, F., Rossi, D., Levita, G., and Marchetti, A., "Dielectric constant enhancement in a silicone elastomer filled with lead magnesium niobate-lead titanate". *Materials Science and Engineering C*, vol. 27, no. 1, pp. 110-116, 2007.
- [84] Zou, C., Fothergill, J. C., and Rowe, S. W., "The effect of water absorption on the dielectric properties of epoxy nanocomposites." *IEEE Transactions on Dielectrics and Electrical Insulation*, vol. 15, no. 1, 106-117, 2008.
- [85] Li, Q., Zhao, T., and Siew, W. H. "Definition and digital algorithms of dielectric loss factor for condition monitoring of high-voltage power equipment with harmonics emphasis". *IEE Proceedings Generation, Transmission and Distribution*, vol. 151, no. 3, pp. 309-312, 2005.
- [86] Roy, M., Nelson, J. K., MacCrone, R. K., and Schadler, L. S. "Candidate mechanisms controlling the electrical characteristics of silica/XLPE nanodielectrics". *Journal of Materials Science*, vol. 42, no. 11, pp. 3789-3799, 2007.
- [87] Barber, P., Balasubramanian, S., Anguchamy, Y., Gong, S., Wibowo, A., Gao, H., Harry, J., Ploehn, H. J., and Zur Loye, H. "Polymer composite and nanocomposite dielectric materials for pulse power energy storage". *Materials*, vol. 2, no. 4, pp. 1697-1733, 2009.
- [88] Tang, H., Lin, Y., and Sodano, H. A. "Enhanced energy storage in nanocomposite capacitors through aligned PZT nanowires by uniaxial strain assembly". *Advanced Energy Materials*, vol. 2, no. 4, pp. 469-476, 2012.
- [89] Jow, T. R. and Cygan, P. J. "Investigation of dielectric breakdown of polyvinylidene fluoride using ac and dc methos". *Proceedings of IEEE International Symposium on Electrical Insulation*, 1992.
- [90] Jow, T. R. and Cygan, P. J. "Dielectric breakdown of polyvinylidene fluoride and its comparisons with other polymers". *Journal of Applied Physics*, vol. 73, no. 10, 1993.

Vita

Miguel Mendoza was born on January 30, 1988 in Ciudad Juarez, Chihuahua, Mexico. He earned his Bachelor of Science in Mechanical Engineering at the University of Texas at El Paso (UTEP) in the spring 2011 semester. Miguel Mendoza continued his graduate career at UTEP where he conducted research in the area of energy storage nanocomposites under Dr. Yirong Lin mentorship. During his graduate studies, he also served as a teaching assistant for the Mechanical Engineering department at UTEP. Up to this date, Miguel Mendoza has published a total of one journal paper and six conference papers.

Permanent address: 7315 Corona del Sol
El Paso, TX, 79911

This thesis was typed by Miguel Mendoza.